

# Neural Parts: Learning Expressive 3D Shape Abstractions with Invertible Neural Networks

Despoina Paschalidou<sup>1,5,6</sup> Angelos Katharopoulos<sup>3,4</sup> Andreas Geiger<sup>1,2,5</sup> Sanja Fidler<sup>6,7,8</sup>

<sup>1</sup>Max Planck Institute for Intelligent Systems Tübingen <sup>2</sup>University of Tübingen

<sup>3</sup>Idiap Research Institute, Switzerland <sup>4</sup>École Polytechnique Fédérale de Lausanne (EPFL)

<sup>5</sup>Max Planck ETH Center for Learning Systems <sup>6</sup>NVIDIA <sup>7</sup>University of Toronto <sup>8</sup>Vector Institute

{firstname.lastname}@tue.mpg.de angelos.katharopoulos@idiap.ch sfidler@nvidia.com

## Abstract

Impressive progress in 3D shape extraction led to representations that can capture object geometries with high fidelity. In parallel, primitive-based methods seek to represent objects as semantically consistent part arrangements. However, due to the simplicity of existing primitive representations, these methods fail to accurately reconstruct 3D shapes using a small number of primitives/parts. We address the trade-off between reconstruction quality and number of parts with Neural Parts, a novel 3D primitive representation that defines primitives using an Invertible Neural Network (INN) which implements homeomorphic mappings between a sphere and the target object. The INN allows us to compute the inverse mapping of the homeomorphism, which in turn, enables the efficient computation of both the implicit surface function of a primitive and its mesh, without any additional post-processing. Our model learns to parse 3D objects into semantically consistent part arrangements without any part-level supervision. Evaluations on ShapeNet, D-FAUST and FreiHAND demonstrate that our primitives can capture complex geometries and thus simultaneously achieve geometrically accurate as well as interpretable reconstructions using an order of magnitude fewer primitives than state-of-the-art shape abstraction methods.

## 1. Introduction

Recovering the geometry of a 3D shape from a single RGB image is a fundamental task in computer vision and graphics. Existing shape reconstruction models utilize a neural network to learn a parametric function that maps the input image into a mesh [52, 37, 45, 91, 96, 65], a point-cloud [28, 73, 2, 44, 87, 96], a voxel grid [9, 16, 30, 75, 77, 84, 94] or an implicit surface [57, 14, 66, 80, 95, 58]. An alternative line of research is focused on compact low-

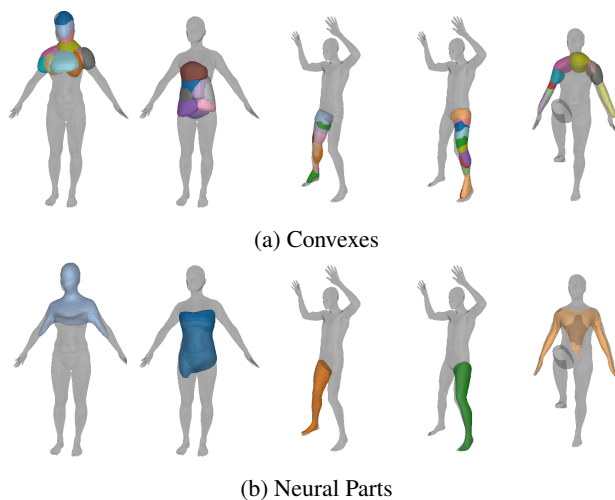


Figure 1: **Expressive Primitives.** We address the trade-off between reconstruction quality and sparsity (i.e. number of parts) in primitive-based methods. Prior work [90, 67, 69, 19] has considered convex shapes as primitives, which due to their simplicity, require a large number of parts to accurately represent complex shapes. This results in less interpretable shape abstractions (i.e. primitives are not identifiable parts e.g. legs, arms etc.). In this work, we propose Neural Parts, a novel 3D primitive representation that can represent arbitrarily complex genus-zero shapes and thus yields geometrically accurate and semantically meaningful parts compared to simpler primitives.

dimensional representations that reconstruct 3D objects by decomposing them into simpler parts, called primitives [90, 67, 19, 34]. Primitive-based representations seek to infer *semantically consistent part arrangements* across different object instances and provide a more interpretable alternative, compared to representations that only focus on capturing the global object geometry. Primitives are particularly useful for various applications where the notion of

parts is necessary, such as shape editing, physics-based applications, graphics simulation etc.

Existing primitive-based methods rely on simple shapes for decomposing complex 3D objects into parts. In the early days of computer vision, researchers explored various shape primitives such as 3D polyhedral shapes [78], generalized cylinders [7] and geons [6] for representing 3D geometries. More recently, the primitive paradigm has been revisited in the context of deep learning and [90, 67, 40, 19] have demonstrated the ability of neural networks to learn part-level geometries using 3D cuboids [90, 62, 99], superquadrics [67], spheres [40] or convexes [19]. Due to their simple parametrization, these primitives have limited expressivity and cannot capture arbitrarily complex geometries. Therefore, existing part-based methods require a large number of primitives for extracting geometrically accurate reconstructions. However, using more primitives comes at the expense of less interpretable reconstructions.

To address this, we devise Neural Parts, a novel 3D primitive representation that is more *expressive* and *interpretable*, in comparison to alternatives that are limited to convex shapes. We argue that a primitive should be a non trivial genus-zero shape with well defined implicit and explicit representations. These characteristics allow us to efficiently combine primitives and accurately represent arbitrarily complex geometries. To this end, we pose the task of primitive learning as the task of learning a *family of homeomorphic mappings* between the 3D space of a simple genus-zero shape (e.g. sphere, cube, ellipsoid) and the 3D space of the target object. We implement this mapping using an Invertible Neural Network (INN) [23]. Being able to map 3D points in both directions allows us to efficiently compute the explicit representation of each primitive, namely its tessellation as well as the implicit representation, i.e. the relative position of a point wrt. the primitive’s surface. In contrast to prior work [90, 67, 19, 69] that directly predict the primitive parameters (i.e. centroids and sizes for cuboids and superquadrics and hyperplanes for convexes), we employ the INN to fully define each primitive. Note that while a homeomorphism preserves the genus of the shape it does not constrain it in any other way. As a result, while existing primitives are constrained to a specific family of shapes (e.g. ellipsoids), our primitives can capture arbitrarily complicated genus-zero shapes (see Fig. 1). We demonstrate that Neural Parts can be learned in an unsupervised fashion (i.e. without any primitive annotations), directly from unstructured 3D point clouds by ensuring that the assembly of predicted primitives accurately reconstructs the target.

In summary, we make the following **contributions**: We propose the first model that defines primitives as a homeomorphic mapping between two topological spaces through conditioning an INN on the input image. Since the homeomorphism does not impose any constraints on the shape

of the predicted primitive, our model effectively decouples geometric accuracy from parsimony and as a result captures complex geometries with an order of magnitude fewer primitives. Experiments on ShapeNet objects [10], D-FAUST humans [8] and FreiHAND hands [98] demonstrate the ability of our model to parse objects into more expressive and semantically meaningful shape abstractions compared to models that rely on simpler primitives [67, 69, 19]. Code and data is publicly available<sup>1</sup>.

## 2. Related Work

Learning-based 3D reconstruction approaches can be categorized based on the type of their output representation to: depth-based [46, 41, 68, 25], voxel-based [16, 93, 30, 75], point-based [28, 73, 2], mesh-based [52, 37, 45], implicit-based [57, 14, 66] and primitive-based [90, 62, 67]. Here, we primarily focus on primitive-based methods that are more relevant to our work. Since our formulation is independent of a specific INN implementation, a thorough discussion of INNs is beyond the scope of this paper, thus we refer the reader to [3] for a detailed overview.

**3D Representations:** Voxels [9, 16, 93, 30, 75, 84, 94] naturally capture the 3D geometry by discretizing the shape into a regular grid. While several efficient space partitioning techniques [56, 77, 86, 39, 76] have been proposed to address their high memory and computation requirements, their application is still limited. A promising new direction explored learning a deformation of the grid itself to better capture geometric details [31]. Point-clouds [28, 73, 2, 44, 87, 96] are more memory efficient but lack surface connectivity, thus post-processing is necessary for generating the final mesh. Most mesh-based methods [52, 37, 45, 91, 96, 35, 65, 11, 19, 97] naturally yield smooth reconstructions but either require a deformable template mesh [91] or represent the geometry as an atlas of multiple mappings [37, 21, 55]. To address these limitations, implicit models [57, 14, 66, 80, 95, 58, 60, 63, 4, 92, 33, 13, 61, 5, 36, 81, 43, 15, 72, 74, 64] have recently gained popularity. These methods represent a 3D shape as the level-set of a distance or occupancy field implemented as a neural network, that takes a context vector and a query point and predicts either a signed distance value [66, 58, 5, 36, 85] or a binary occupancy value [57, 14] for the query point. While these methods result in accurate reconstructions, they lack interpretability as they do not consider the part-based object structure. Instead, we focus on part-based representations and showcase that our model simultaneously yields geometrically accurate and interpretable reconstructions. Furthermore, in contrast to implicit models, that require expensive iso-surfacing operations (i.e. marching cubes) to extract a mesh, our model directly predicts a high resolution mesh

<sup>1</sup>[https://paschalidoud.github.io/neural\\_parts](https://paschalidoud.github.io/neural_parts)

for each part, without any post-processing.

**Structured-based Representations:** Our work falls into the category of shape abstraction techniques. This line of research seeks to decompose 3D shapes into semantically meaningful simpler parts using either supervision in terms of the primitive parameters [99, 62, 49, 59, 32, 50, 83, 51] or without any part-level annotations [90, 67, 22, 69, 34, 19, 47]. Neural Parts perform primitive-based learning in an unsupervised manner. Traditional primitives include cuboids [90, 62, 99, 49, 59, 26], superquadrics [67, 69], convexes [19, 12, 29], CSG trees [82] or shape programmings [27, 88, 53]. Due to the simplicity of the shapes of traditional primitives, the reconstruction quality of existing part-based methods is coupled with the number of primitives, namely a larger number of primitives results in more accurate reconstructions (see Fig. 5). However, these reconstructions are less parsimonious and the constituent primitives often lack a semantic interpretation (i.e. are not recognizable parts). Instead, Neural Parts are not restricted to convex shapes and can capture complex geometries with a few primitives. In recent work, [33] propose a 3D representation that decomposes space into a structured set of implicit functions [34]. However, extracting a single part from their prediction is not possible. This is not the case for our model.

**Shape Deformations:** Deforming a single genus-zero shape into more complicated shapes with graph convolutions [91], MLPs [37, 89] and Neural ODEs [38] has demonstrated impressive results. Groueix et al. [37] were among the first to employ an MLP to implement a homeomorphism between a sphere and a complicated shape. Note that since the deformation is implemented via an MLP, computing the inverse mapping becomes infeasible. Very recently, [38] proposed to learn the deformation of a single ellipsoid using several Neural ODEs. Similar to our Neural Parts, their model is invertible, however it does not consider any part decomposition or latent object structure. Instead, we use the inverse mapping of the homeomorphism to define the predicted shape as the union of primitives, by discarding points from a part’s surface that are internal to any other part. Thus our model learns to combine multiple genus-zero primitives and is able to reconstruct shapes of arbitrary genus. In addition, we formulate our losses using the forward and the inverse mapping of the homeomorphism, which in turn, allows us to utilize both volumetric as well as surface information during training. This facilitates imposing additional constraints on the predicted primitives e.g. normal consistency and parsimony and leads to more accurate results as evidenced by our experiments.

### 3. Method

Given an input image we seek to learn a representation with  $M$  primitives that best describes the target object. We

define our primitives via a *deformation between shapes* that is parametrized as a *learned homeomorphism* implemented with an Invertible Neural Network (INN). Using an INN allows us to efficiently compute the implicit and explicit representation of the predicted shape and impose various constraints on the predicted parts.

In particular, for each primitive, we seek to learn a homeomorphism between the 3D space of a simple genus-zero shape and the 3D space of the target object, such that the deformed shape matches a part of the target object. Due to its simple implicit surface definition and tessellation, we employ a sphere as our genus-zero shape. We refer to the 3D space of the sphere as *latent space* and to the 3D space of the target object as *primitive space*.

In Sec. 3.1, we present the explicit and implicit representation of our primitives as a homeomorphism of a sphere. Subsequently, in Sec. 3.2, we present our novel architecture for predicting multiple primitives using homeomorphisms conditioned on the input image. Finally, in Sec. 3.3, we formulate our optimization objective.

#### 3.1. Primitives as Homeomorphic Mappings

A homeomorphism is a continuous map between two topological spaces  $Y$  and  $X$  that preserves all topological properties. Intuitively a homeomorphism is a continuous stretching and bending of  $Y$  into a new space  $X$ . In our 3D topology, a homeomorphism  $\phi_\theta : \mathbb{R}^3 \rightarrow \mathbb{R}^3$  is

$$\mathbf{x} = \phi_\theta(\mathbf{y}) \text{ and } \mathbf{y} = \phi_\theta^{-1}(\mathbf{x}) \quad (1)$$

where  $\mathbf{x}$  and  $\mathbf{y}$  are 3D points in  $X$  and  $Y$  and  $\phi_\theta : Y \rightarrow X$ ,  $\phi_\theta^{-1} : X \rightarrow Y$  are continuous bijections. In our setting,  $Y$  and  $X$  correspond to the latent and the primitive space respectively. Using the explicit and implicit representation of a sphere with radius  $r$ , positioned at  $(0, 0, 0)$  and the homeomorphic mapping from (1), we can now define the implicit and explicit representation of a single primitive.

**Explicit Representation:** The explicit representation of a primitive, parametrized as a mesh with vertices  $\mathcal{V}_p$  and faces  $\mathcal{F}_p$ , can be obtained by applying the homeomorphism on the sphere vertices  $\mathcal{V}$  and faces  $\mathcal{F}$  as follows:

$$\begin{aligned} \mathcal{V}_p &= \{\phi_\theta(\mathbf{v}_j), \forall \mathbf{v}_j \in \mathcal{V}\} \\ \mathcal{F}_p &= \mathcal{F}. \end{aligned} \quad (2)$$

It is evident that applying  $\phi_\theta$  on the sphere vertices  $\mathcal{V}$  alters their location in the primitive space, while the vertex arrangements (i.e. faces) remain unchanged. Since our primitives are defined as a deformation of a sphere mesh of arbitrarily high resolution, we can also obtain primitive meshes of arbitrary resolutions without any post-processing, such as marching-cubes which is required for traditional neural implicit representations [57].

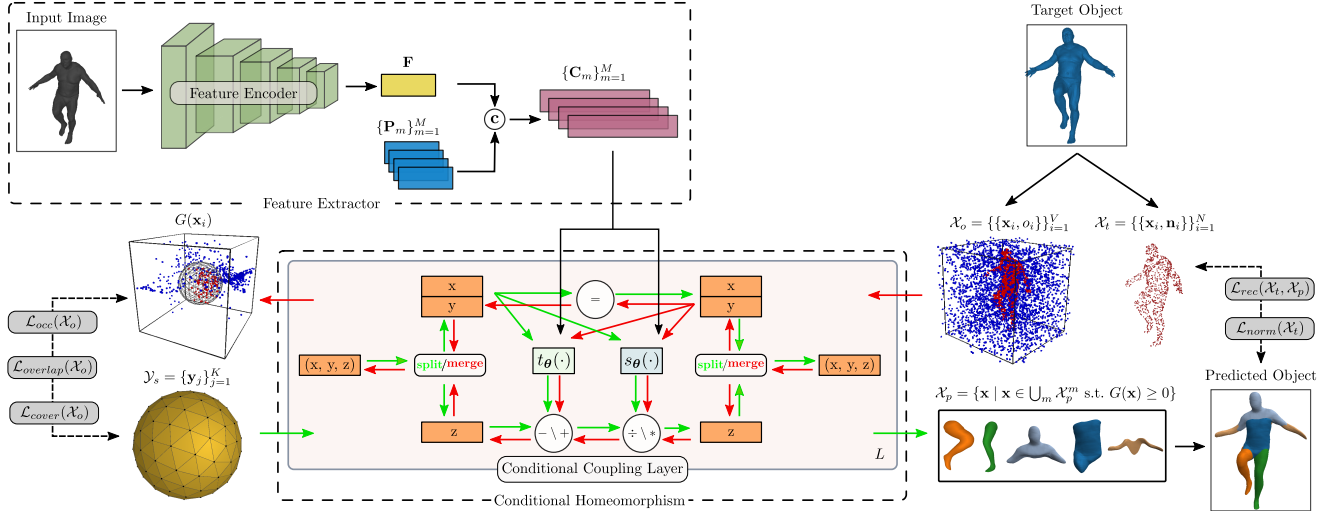


Figure 2: **Method Overview.** Our model comprises two main components: A *Feature Extractor* which maps an input image into a per-primitive shape embedding and a *Conditional Homeomorphism* that deforms a sphere into  $M$  primitives and vice-versa. First, the *feature encoder* maps the input to a global feature representation  $\mathbf{F}$ . Then, for every primitive  $m$ ,  $\mathbf{F}$  is concatenated with a learnable primitive embedding  $\mathbf{P}_m$  to generate the shape embedding  $\mathbf{C}_m$  for this primitive. The *Conditional Homeomorphism*  $\phi_{\theta}(\cdot; \mathbf{C}_m)$  is implemented by a stack of  $L$  conditional coupling layers. Applying the *forward mapping* on a set of points  $\mathcal{Y}_s$ , randomly sampled on the surface of the sphere, generates points on the surface of the  $m$ -th primitive  $\mathcal{X}_p^m$  (9). Using the *inverse mapping*  $\phi_{\theta}^{-1}(\cdot; \mathbf{C}_m)$ , allows us to compute whether any point in 3D space lies inside or outside a primitive (7). We train our model using both *surface* ( $\mathcal{L}_{rec}, \mathcal{L}_{norm}$ ) and *occupancy* ( $\mathcal{L}_{occ}$ ) losses to simultaneously capture fine object details and volumetric characteristics of the target object. The use of the *inverse mapping* allows us to impose additional constraints (e.g. discouraging inter-penetration) on the predicted primitives ( $\mathcal{L}_{overlap}, \mathcal{L}_{cover}$ ).

**Implicit Representation:** The implicit representation of a primitive can be derived by applying the inverse homeomorphic mapping on a 3D point  $\mathbf{x}$  as follows

$$g(\mathbf{x}) = \|\phi_{\theta}^{-1}(\mathbf{x})\|_2 - r. \quad (3)$$

To evaluate the relative position of a point  $\mathbf{x}$  wrt. the primitive surface it suffices to evaluate whether  $\phi_{\theta}^{-1}(\mathbf{x})$  lies inside, outside or on the surface of the sphere. Namely, points that are internal to the sphere are also inside the primitive and points that are outside the sphere are also outside the primitive surface. Note that computing  $g(\mathbf{x})$  in (3) is only possible because  $\phi_{\theta}(\mathbf{x})$  is implemented with an INN.

**Multiple Primitives:** The homeomorphism in (1) implements a single deformation. However, we seek to predict multiple primitives (i.e. deformations) conditioned on the input. Hence, we define a conditional homeomorphism as:

$$\mathbf{x} = \phi_{\theta}(\mathbf{y}; \mathbf{C}_m) \text{ and } \mathbf{y} = \phi_{\theta}^{-1}(\mathbf{x}; \mathbf{C}_m) \quad (4)$$

where  $\mathbf{C}_m$  is the shape embedding for the  $m$ -th primitive and is predicted from the input. Note that for different shape embeddings a different homeomorphism is defined.

### 3.2. Network Architecture

Our architecture comprises two main components: (i) the *feature extractor* that maps the input to a vector of per-

primitive shape embeddings  $\{\mathbf{C}_m\}_{m=1}^M$  and (ii) the *conditional homeomorphism* that learns a homeomorphic mapping conditioned on the shape embedding. The overall architecture is illustrated in Fig. 2.

**Feature Extractor:** The first part of the feature extractor module is a ResNet-18 [42] that extracts a feature representation  $\mathbf{F} \in \mathbb{R}^D$  from the input image. Subsequently, for every primitive  $m$ ,  $\mathbf{F}$  is concatenated with a learnable primitive embedding  $\mathbf{P}_m \in \mathbb{R}^D$  to derive a shape embedding  $\mathbf{C}_m \in \mathbb{R}^{2D}$  for this primitive.

**Conditional Homeomorphism:** We implement the INN using a Real NVP [24] due to its simple formulation. A Real NVP models a bijective mapping by stacking a sequence of simple bijective transformation functions. For each bijection, typically referred to as *affine coupling layer*, given an input 3D point  $(x_i, y_i, z_i)$ , the output point  $(x_o, y_o, z_o)$  is

$$\begin{aligned} x_o &= x_i \\ y_o &= y_i \\ z_o &= z_i \exp(s_{\theta}(x_i, y_i)) + t_{\theta}(x_i, y_i) \end{aligned} \quad (5)$$

where  $s_{\theta} : \mathbb{R}^2 \rightarrow \mathbb{R}$  and  $t_{\theta} : \mathbb{R}^2 \rightarrow \mathbb{R}$  are *scale* and *translation* functions implemented with two arbitrarily complicated networks. Namely, in each bijection, the input is

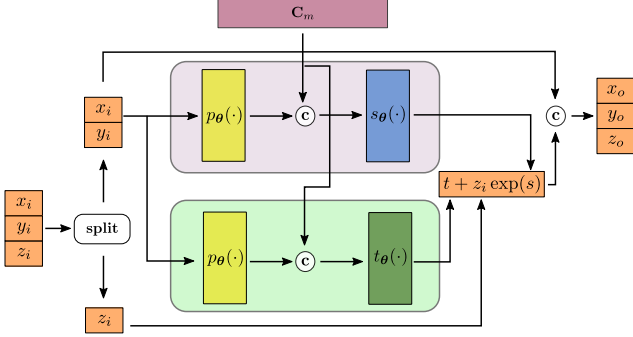


Figure 3: **Conditional Coupling Layer.** Pictorial representation of (20). The input point  $(x_i, y_i, z_i)$  is passed into a *coupling layer* that scales and translates one dimension of the input based on the other two and the per-primitive shape embedding  $\mathbf{C}_m$ . The scale factor  $s$  and the translation amount  $t$  are predicted by two MLPs,  $s_\theta(\cdot)$  and  $t_\theta(\cdot)$ .  $p_\theta(\cdot)$  is another MLP that increases the dimensionality of the input point before it is concatenated with  $\mathbf{C}_m$ .

split into two,  $(x_i, y_i)$  and  $z_i$ . The first part remains unchanged and the second undergoes an affine transformation with  $s_\theta(\cdot)$  and  $t_\theta(\cdot)$ . We follow [24] and we enforce that consecutive affine coupling layers scale and translate different input dimensions. Namely, we alternate the splitting between the dimensions of the input randomly.

However, the original Real NVP cannot be directly applied in our setting as it does not consider a shape embedding. To address this, we augment the affine coupling layer as follows: we first map  $(x_i, y_i)$  into a higher dimensional feature vector using a mapping,  $p_\theta(\cdot)$ , implemented as an MLP. This is done to increase the relative importance of the input point before concatenating it with the high-dimensional shape embedding  $\mathbf{C}_m$ . The *conditional affine coupling layer* becomes

$$\begin{aligned} x_o &= x_i \\ y_o &= y_i \\ z_o &= z_i \exp(s_\theta([\mathbf{C}_m; p_\theta(x_i, y_i)])) \\ &\quad + t_\theta([\mathbf{C}_m; p_\theta(x_i, y_i)]) \end{aligned} \quad (6)$$

where  $[\cdot; \cdot]$  denotes concatenation. A graphical representation of our conditional coupling layer is provided in Fig. 3.

### 3.3. Training

Due to the lack of primitive annotations, we train our model by minimizing the geometric distance between the target and the predicted shape. Our supervision comes from a watertight mesh of the target object. In the following, we define the implicit and explicit representation of the predicted shape as the union of  $M$  primitives.

The implicit surface of the  $m$ -th primitive can be derived from (3), by applying the inverse homeomorphic mapping

on points in 3D space:

$$g^m(\mathbf{x}) = \|\phi_\theta^{-1}(\mathbf{x}; \mathbf{C}_m)\|_2 - r, \quad \forall \mathbf{x} \in \mathbb{R}^3 \quad (7)$$

We define the implicit surface representation of the entire object as the union of all per-primitive implicit functions

$$G(\mathbf{x}) = \min_{m \in 0 \dots M} g^m(\mathbf{x}), \quad (8)$$

namely we consider that a point is inside the predicted shape if it is inside at least one primitive.

Similarly, the explicit representation of the  $m$ -th primitive is a set of points on its surface, let it be  $\mathcal{X}_p^m$ , that are generated by applying the forward homeomorphic mapping on points on the sphere surface  $\mathcal{Y}_s$  in the latent space

$$\mathcal{X}_p^m = \{\phi_\theta(\mathbf{y}_j; \mathbf{C}_m), \quad \forall \mathbf{y}_j \in \mathcal{Y}_s\}. \quad (9)$$

To generate points on the surface of the predicted shape  $\mathcal{X}_p$ , we first need to generate points on the surface of each primitive and then discard the ones that are inside any other primitive. From (8) this can be expressed as follows:

$$\mathcal{X}_p = \{\mathbf{x} \mid \mathbf{x} \in \bigcup_m \mathcal{X}_p^m \text{ s.t. } G(\mathbf{x}) \geq 0\}. \quad (10)$$

**Loss Functions:** Our loss  $\mathcal{L}$  seeks to minimize the geometric distance between the target and the predicted shape and is composed of five loss terms:

$$\begin{aligned} \mathcal{L} &= \mathcal{L}_{rec}(\mathcal{X}_t, \mathcal{X}_p) + \mathcal{L}_{occ}(\mathcal{X}_o) + \mathcal{L}_{norm}(\mathcal{X}_t) \\ &\quad + \mathcal{L}_{overlap}(\mathcal{X}_o) + \mathcal{L}_{cover}(\mathcal{X}_o) \end{aligned} \quad (11)$$

where  $\mathcal{X}_t = \{\{\mathbf{x}_i, \mathbf{n}_i\}\}_{i=1}^N$  comprises surface samples of the target shape and the corresponding normals, and  $\mathcal{X}_o = \{\{\mathbf{x}_i, o_i\}\}_{i=1}^V$  denotes a set of occupancy pairs, where  $\mathbf{x}_i$  corresponds to the location of the  $i$ -th point and  $o_i$  denotes whether  $\mathbf{x}_i$  lies inside ( $o_i = 1$ ) or outside ( $o_i = 0$ ) the target. Note that our optimization objective comprises both occupancy (13) and surface losses (12)+(14), since they model complementary characteristics of the target object e.g. the surface loss attends to fine details that may have small volume, whereas the occupancy loss more efficiently models empty space. We empirically observe that using both significantly improves reconstruction (see Sec. 4.3).

**Reconstruction Loss:** We measure the surface reconstruction quality using a bidirectional Chamfer loss between the points  $\mathcal{X}_p$  on the surface of the predicted shape and the points on the target object  $\mathcal{X}_t$  as follows:

$$\begin{aligned} \mathcal{L}_{rec}(\mathcal{X}_t, \mathcal{X}_p) &= \frac{1}{|\mathcal{X}_t|} \sum_{\mathbf{x}_i \in \mathcal{X}_t} \min_{\mathbf{x}_j \in \mathcal{X}_p} \|\mathbf{x}_i - \mathbf{x}_j\|_2^2 + \\ &\quad \frac{1}{|\mathcal{X}_p|} \sum_{\mathbf{x}_j \in \mathcal{X}_p} \min_{\mathbf{x}_i \in \mathcal{X}_t} \|\mathbf{x}_i - \mathbf{x}_j\|_2^2 \end{aligned} \quad (12)$$

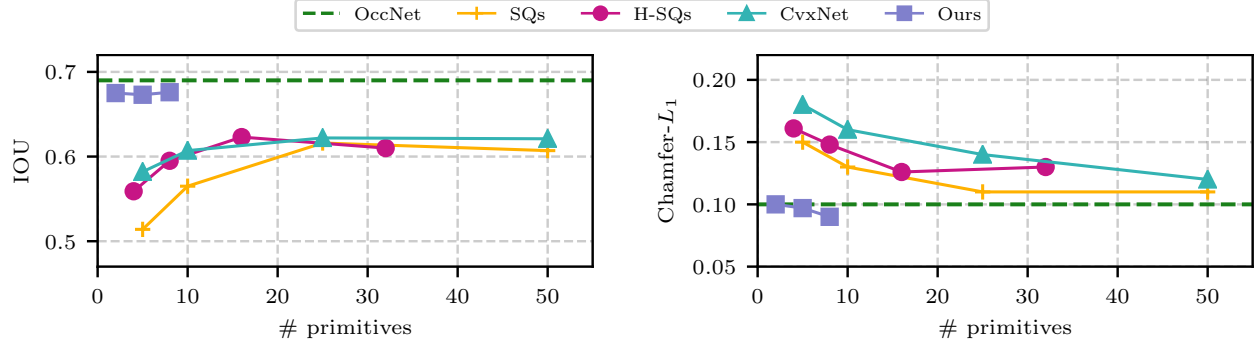


Figure 4: **Trade-off Reconstruction Quality and # Primitives.** We evaluate the reconstruction quality of primitive-based methods on the D-FAUST test set for different number of primitives. Neural Parts (purple) outperform CvxNet (turquoise), SQs (orange) and H-SQs (magenta) in terms of both IoU ( $\uparrow$ ) and Chamfer-L1 ( $\downarrow$ ) for any primitive configuration, even when using as little as 2 primitives. In addition, we show that our reconstructions are competitive to OccNet (dashed) which does not provide a primitive-based representation and requires expensive post-processing for extracting surface meshes.

The first term of (12) measures the completeness of the predicted shape, namely the average distance of all ground truth points to the closest predicted points. The second term measures its accuracy, namely the average distance of all predicted points to the closest ground-truth points.

**Occupancy Loss:** The occupancy loss ensures that the volume of the predicted shape matches the volume of the target. Intuitively, we want to ensure that the free and the occupied space of the predicted and the target object coincide. To this end, we convert the implicit surface of the predicted shape from (8) to an indicator function and compute the binary cross-entropy loss

$$\mathcal{L}_{occ}(\mathcal{X}_o) = \sum_{(\mathbf{x}, o) \in \mathcal{X}_o} \mathcal{L}_{ce} \left( \sigma \left( \frac{-G(\mathbf{x})}{\tau} \right), o \right), \quad (13)$$

which we sum over all volume samples  $\mathcal{X}_o$ . Here,  $\mathcal{L}_{ce}(\cdot, \cdot)$  is the cross-entropy classification loss,  $\sigma(\cdot)$  is the sigmoid function and  $\tau$  is a temperature hyperparameter that defines the sharpness of the boundary of the indicator function. Note that  $\sigma \left( \frac{-G(\mathbf{x})}{\tau} \right)$  is 1 when  $\mathbf{x}$  is inside the predicted shape and 0 otherwise.

**Normal Consistency Loss:** The normal consistency loss ensures that the orientation of the normals of the predicted shape will be aligned with the normals of the target. We penalize misalignments between the predicted and the target normals by minimizing the cosine distance as follows

$$\mathcal{L}_{norm}(\mathcal{X}_t) = \frac{1}{|\mathcal{X}_t|} \sum_{(\mathbf{x}, \mathbf{n}) \in \mathcal{X}_t} \left( 1 - \left\langle \frac{\nabla_{\mathbf{x}} G(\mathbf{x})}{\|\nabla_{\mathbf{x}} G(\mathbf{x})\|_2}, \mathbf{n} \right\rangle \right) \quad (14)$$

where  $\langle \cdot, \cdot \rangle$  is the dot product. Note that the surface normal of the predicted shape for a point  $\mathbf{x}$  is simply the gradient of the implicit surface wrt. to point  $\mathbf{x}$  and can be efficiently computed with automatic differentiation.

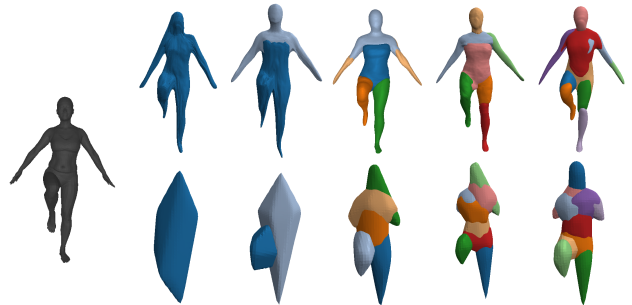


Figure 5: **Human body modelling.** We visualize the target mesh and the predicted primitives with Neural Parts (first row) and CvxNet (second) using 1, 2, 5, 8 and 10 primitives.

**Overlapping Loss:** To encourage semantically meaningful shape abstractions, where primitives represent different object parts, we introduce a non-overlapping loss that penalizes any point in space that is internal to more than  $\lambda$  primitives as follows:

$$\mathcal{L}_{overlap}(\mathcal{X}_o) = \frac{1}{|\mathcal{X}_o|} \max \left( 0, \sum_{m=1}^M \sigma \left( \frac{-g^m(\mathbf{x})}{\tau} \right) - \lambda \right) \quad (15)$$

**Coverage Loss:** The coverage loss makes sure that all primitives cover parts of the predicted shape. In practice, it prevents degenerate primitive arrangements, where some primitives are very small and do not contribute to the reconstruction. We implement this loss by encouraging that each primitive contains at least  $k$  points of the target object:

$$\mathcal{L}_{cover}(\mathcal{X}_o) = \sum_{m=1}^M \sum_{\mathbf{x} \in \mathcal{N}_k^m} \max(0, g^m(\mathbf{x})). \quad (16)$$

Here  $\mathcal{N}_k^m \subset \{(\mathbf{x}, o) \in \mathcal{X}_o | o = 1\}$  contains the  $k$  points with the minimum distance from the  $m$ -th primitive.

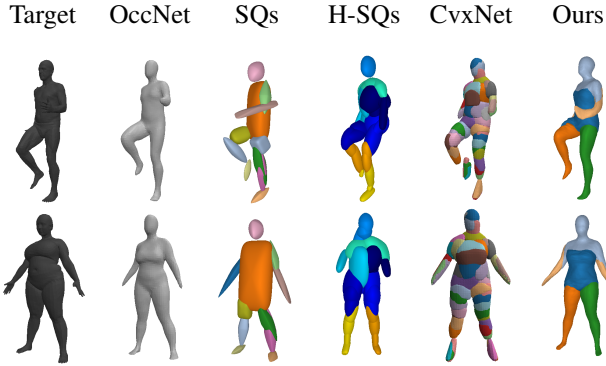


Figure 6: **Single Image 3D Reconstruction on D-FAUST.** The input image is shown on the first column and the rest contain predictions of all methods: OccNet (second), primitive-based predictions with superquadrics (third and fourth) and convexes (fifth) and ours with 5 primitives (last).

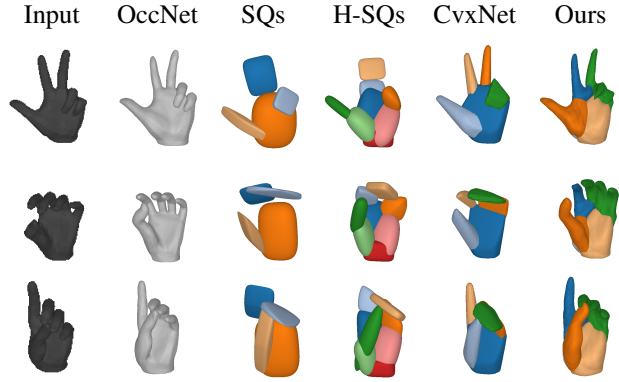
## 4. Experimental Evaluation

**Datasets:** We report results on three different datasets: D-FAUST [8], FreiHAND [98] and ShapeNet [10]. D-FAUST contains 38,640 meshes of humans performing various tasks such as “chicken wings” and “running on spot”. For ShapeNet [10], we perform category specific training using the same image renderings and train/test splits as [16]. Finally, for FreiHAND [98], we select the first 5000 hand poses and generate meshes using the provided MANO parameters [79]. Details regarding data preprocessing and additional results are provided in the supplementary.

**Baselines:** We compare against various primitive-based methods: SQs [67] that employ superquadrics, CvxNet [19] that use smooth convexes and H-SQs [69] that consider a hierarchical, geometrically more accurate decomposition of parts using superquadrics. Finally, we also report results for OccNet [57], a state-of-the-art implicit-based method that does not reason about object parts. For all baselines, we use the code provided by the authors.

### 4.1. Representation Power

To evaluate the representation power of Neural Parts, we train our model and our baselines on D-FAUST for different number of primitives and measure their reconstruction quality. In particular, we train our model for 2, 5 and 8 primitives, CvxNet [19] and SQs [67] for 5, 10, 25 and 50 primitives and H-SQs [69] for 4, 8, 16 and 32 primitives. In Fig. 4, we report the reconstruction performance wrt. IoU and Chamfer- $L_1$  distance. Neural Parts achieve more accurate reconstructions for any given number of primitives and are competitive to OccNet that does not reason about parts. In particular, our model achieves 67.3% IOU with only 5 primitives, whereas CvxNet, with 10 times more primitives, achieve 62%. This is also validated qualitatively in Fig. 5, where we compare the predictions of CvxNet and our model



	OccNet	SQs	H-SQs	CvxNet	Ours
IoU	0.891	0.693	0.768	0.832	<b>0.879</b>
Chamfer- $L_1$	0.038	0.093	0.077	0.059	<b>0.057</b>

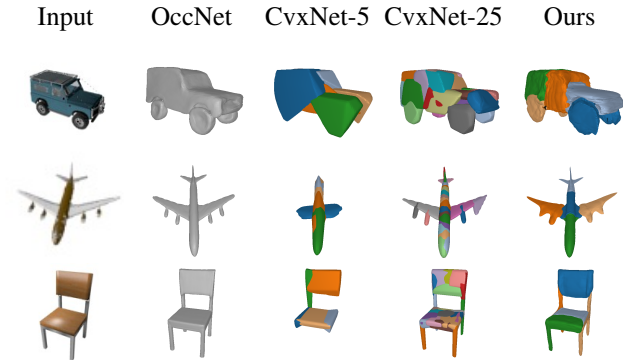
Figure 7: **Single Image 3D Reconstruction on FreiHAND.** We compare our model with OccNet, SQs and CvxNet with 5 primitives and H-SQs with 8 primitives. Our model outperforms all primitive based methods in terms of both IoU ( $\uparrow$ ) and Chamfer- $L_1$  ( $\downarrow$ ) distance.

for different number of primitives. Neural Parts accurately capture the pose and the limbs of the human with as little as one or two primitives, whereas CvxNet fail to reconstruct the arms even with 10 primitives.

### 4.2. Reconstruction Accuracy

**Dynamic FAUST:** In this experiment, we compare CvxNet and SQs with 50 primitives and H-SQs for a maximum number of 32 primitives to Neural Parts with 5 primitives to showcase that our model can capture the human body’s geometry using an order of magnitude less primitives. Qualitative results from the predicted primitives using our model and the baselines are summarized in Fig. 6. Note that OccNet is not directly comparable with part-based methods, however, we include it in our analysis as a typical representative of powerful implicit shape extraction techniques. We observe that while all methods roughly capture the human pose, Neural Parts result in a part assembly that is very close to the target object. While CvxNet with 50 primitives yield fairly accurate reconstructions, the final representation lacks any part-level semantic interpretation. The quantitative evaluation of this experiment is provided in Fig. 4.

**FreiHAND:** For this experiment, we train our model, CvxNet and SQs with 5 and H-SQs with 8 primitives. Fig. 7 summarizes the reconstruction performance for all methods. We observe that Neural Parts yield more geometrically accurate reconstructions that faithfully capture fine details, i.e. the position of the thumb, (see Fig. 7) whereas CvxNet and SQs focus primarily on the structure of the predicted shape and miss out fine details.



IoU	OccNet	CvxNet - 5	CvxNet - 25	Ours
cars	0.763	0.650	0.666	<b>0.697</b>
planes	0.451	0.425	0.448	<b>0.454</b>
chairs	0.432	0.364	0.392	<b>0.412</b>

Figure 8: **Single Image 3D Reconstruction on ShapeNet.** We compare Neural Parts to OccNet and CvxNet with 5 and 25 primitives. Our model yields semantic and more accurate reconstructions with  $5\times$  less primitives.

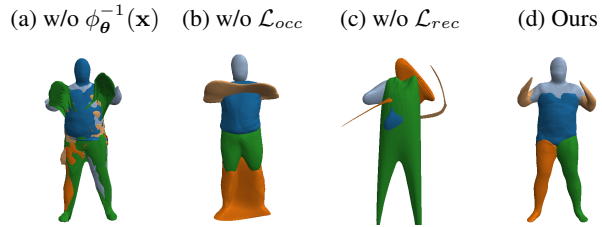
**ShapeNet:** We train Neural Parts with 5 primitives and CvxNet with 5 and 25 primitives on various ShapeNet objects. We observe that our model results in more accurate reconstructions than CvxNet with both 5 and 25 primitives (see Fig. 8). When increasing the number of primitives to 25, CvxNet improves in terms of reconstruction quality but the predicted primitives lack semantic interpretation. Furthermore, for the case of chairs, CvxNet with 5 primitives do not have enough representation power, thus entire object parts are missing. Additional results as well as comparison wrt. Chamfer- $L_1$  distance are provided in the supplementary.

### 4.3. Ablation Study

In this section, we train our model on D-FAUST with 5 primitives and investigate the impact of its components. Additional ablations are provided in the supplementary.

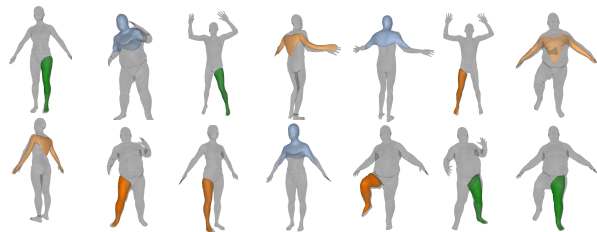
**Invertibility:** To investigate the impact of the INN, we train our model without using the inverse mapping,  $\phi_{\theta}^{-1}(\mathbf{x})$ . As a result, it is not possible to either compute the union of parts or enforce additional constraints on the predicted primitives i.e. we only train with the loss of (12), without discarding internal points as in (9). From Fig. 9a it becomes evident that each primitive seeks to cover the entire shape thus resulting in redundant and non semantic primitives. In addition, the lack of an inverse mapping prevents us from using any occupancy loss, which results in poor modelling of empty space (i.e. the hands are connected with the body).

**Occupancy and Surface Losses:** We compare the performance of our model using either the occupancy (13) or the surface loss (12). The reconstruction without  $\mathcal{L}_{occ}$



	w/o $\phi_{\theta}^{-1}(\mathbf{x})$	w/o $\mathcal{L}_{occ}$	w/o $\mathcal{L}_{rec}$	Ours
IoU	0.639	0.642	0.643	0.673
Chamfer- $L_1$	0.119	0.125	0.150	0.09

Figure 9: **Ablation Study.** We ablate the INN as well as the volumetric and the surface loss and show their impact both quantitatively and qualitatively.



	L-thumb	R-thumb	L-toe	R-toe	Nose
CvxNet-5	61.1%	67.1%	98.2%	91.2%	98%
CvxNet-50	29%	37%	56.3%	58.1%	52%
Ours	91.9%	88.2%	99.8%	92.5%	100%

Figure 10: **Semantic Consistency.** We report the classification accuracy of semantic vertices on the human body using the label of the closest primitive. Our predicted primitives are consistently used for representing the same human part.

(Fig. 9b) accurately captures the geometry of the human but fails to efficiently model empty space (i.e. legs are connected). Similarly, the reconstruction without  $\mathcal{L}_{rec}$  (Fig. 9c) results in degenerate primitives with small volume that are “pushed” far away from the human body.

**Semantic Consistency:** We now investigate the ability of our model to decompose 3D objects into semantically consistent parts. Similar to [19], we use 5 representative vertex indices provided by SMPL-X [71] (i.e. thumbs, toes and nose) and compute the classification accuracy of those points when using the label of the closest primitive. We compare with CvxNet with 5 and 50 primitives and note that Neural Parts are more semantically consistent (see Fig. 10).

## 5. Conclusion

We consider this paper as a step towards bridging the gap between interpretable and high fidelity primitive-based reconstructions. Our experiments demonstrate the ability of our model to learn geometrically accurate reconstructions

that preserve the semantic interpretation of each part. In addition, we show that our expressive primitives outperform existing methods, that rely on simple shapes, both in terms of accuracy and semanticness. In future work, we plan to investigate learning primitive-based decompositions without access to target meshes using differentiable rendering techniques. In addition, we aim to investigate replacing the sphere with more complex shapes in order to obtain even more expressive primitives.

## Acknowledgments

This research was supported by the Max Planck ETH Center for Learning Systems and an NVIDIA research gift.

## References

- [1] Martín Abadi, Paul Barham, Jianmin Chen, Zhifeng Chen, Andy Davis, Jeffrey Dean, Matthieu Devin, Sanjay Ghemawat, Geoffrey Irving, Michael Isard, Manjunath Kudlur, Josh Levenberg, Rajat Monga, Sherry Moore, Derek Gordon Murray, Benoit Steiner, Paul A. Tucker, Vijay Vasudevan, Pete Warden, Martin Wicke, Yuan Yu, and Xiaoqiang Zhang. Tensorflow: A system for large-scale machine learning. *arXiv.org*, 1605.08695, 2016. [16](#)
- [2] Panos Achlioptas, Olga Diamanti, Ioannis Mitliagkas, and Leonidas J. Guibas. Learning representations and generative models for 3d point clouds. In *Proc. of the International Conf. on Machine Learning (ICML)*, 2018. [1](#), [2](#)
- [3] Lynton Ardizzone, Jakob Kruse, Carsten Rother, and Ullrich Köthe. Analyzing inverse problems with invertible neural networks. In *Proc. of the International Conf. on Learning Representations (ICLR)*, 2019. [2](#)
- [4] Matan Atzmon, Niv Haim, Lior Yariv, Ofer Israelov, Haggai Maron, and Yaron Lipman. Controlling neural level sets. In *Advances in Neural Information Processing Systems (NIPS)*, 2019. [2](#)
- [5] Matan Atzmon and Yaron Lipman. SAL: sign agnostic learning of shapes from raw data. In *Proc. IEEE Conf. on Computer Vision and Pattern Recognition (CVPR)*, pages 2562–2571, 2020. [2](#)
- [6] Irving Biederman. Human image understanding: Recent research and a theory. *Computer Vision, Graphics, and Image Processing*, 1986. [2](#)
- [7] I Binford. Visual perception by computer. In *IEEE Conference of Systems and Control*, 1971. [2](#)
- [8] Federica Bogo, Javier Romero, Gerard Pons-Moll, and Michael J. Black. Dynamic FAUST: registering human bodies in motion. In *Proc. IEEE Conf. on Computer Vision and Pattern Recognition (CVPR)*, 2017. [2](#), [7](#), [13](#), [24](#)
- [9] André Brock, Theodore Lim, James M. Ritchie, and Nick Weston. Generative and discriminative voxel modeling with convolutional neural networks. *arXiv.org*, 1608.04236, 2016. [1](#), [2](#)
- [10] Angel X. Chang, Thomas A. Funkhouser, Leonidas J. Guibas, Pat Hanrahan, Qi-Xing Huang, Zimo Li, Silvio Savarese, Manolis Savva, Shuran Song, Hao Su, Jianxiong Xiao, Li Yi, and Fisher Yu. Shapenet: An information-rich 3d model repository. *arXiv.org*, 1512.03012, 2015. [2](#), [7](#), [13](#), [27](#)
- [11] Wenzheng Chen, Huan Ling, Jun Gao, Edward Smith, Jaako Lehtinen, Alec Jacobson, and Sanja Fidler. Learning to predict 3d objects with an interpolation-based differentiable renderer. In *Advances in Neural Information Processing Systems (NIPS)*, 2019. [2](#)
- [12] Zhiqin Chen, Andrea Tagliasacchi, and Hao Zhang. Bsp-net: Generating compact meshes via binary space partitioning. In *Proc. IEEE Conf. on Computer Vision and Pattern Recognition (CVPR)*, pages 42–51, 2020. [3](#)
- [13] Zhiqin Chen, Kangxue Yin, Matthew Fisher, Siddhartha Chaudhuri, and Hao Zhang. BAE-NET: branched autoencoder for shape co-segmentation. In *Proc. of the IEEE International Conf. on Computer Vision (ICCV)*, 2019. [2](#)
- [14] Zhiqin Chen and Hao Zhang. Learning implicit fields for generative shape modeling. In *Proc. IEEE Conf. on Computer Vision and Pattern Recognition (CVPR)*, 2019. [1](#), [2](#)
- [15] Julian Chibane, Thiemo Alldieck, and Gerard Pons-Moll. Implicit functions in feature space for 3d shape reconstruction and completion. In *Proc. IEEE Conf. on Computer Vision and Pattern Recognition (CVPR)*, 2020. [2](#)
- [16] Christopher Bongsoo Choy, Danfei Xu, JunYoung Gwak, Kevin Chen, and Silvio Savarese. 3d-r2n2: A unified approach for single and multi-view 3d object reconstruction. In *Proc. of the European Conf. on Computer Vision (ECCV)*, 2016. [1](#), [2](#), [7](#), [27](#)
- [17] A. H. J. Christensen. A note on geodesic polyhedra: Triangulation and contouring of spheres. *Comput. Graph.*, 3(4):163–165, 1978. [15](#)
- [18] Boyang Deng, Kyle Genova, Soroosh Yazdani, Sofien Bouaziz, Geoffrey Hinton, and Andrea Tagliasacchi. Cvxnets: Learnable convex decomposition. *arXiv.org*, 2019. [24](#)
- [19] Boyang Deng, Kyle Genova, Soroosh Yazdani, Sofien Bouaziz, Geoffrey Hinton, and Andrea Tagliasacchi. Cvxnets: Learnable convex decomposition. *Proc. IEEE Conf. on Computer Vision and Pattern Recognition (CVPR)*, 2020. [1](#), [2](#), [3](#), [7](#), [8](#), [16](#), [28](#), [29](#), [30](#), [31](#)
- [20] Jia Deng, Wei Dong, Richard Socher, Li jia Li, Kai Li, and Li Fei-fei. Imagenet: A large-scale hierarchical image database. In *Proc. IEEE Conf. on Computer Vision and Pattern Recognition (CVPR)*, 2009. [13](#)
- [21] Zhantao Deng, Jan Bednařík, Mathieu Salzmann, and Pascal Fua. Better patch stitching for parametric surface reconstruction. 2020. [2](#)
- [22] Theo Deprelle, Thibault Groueix, Matthew Fisher, Vladimir G Kim, Bryan C Russell, and Mathieu Aubry. Learning elementary structures for 3d shape generation and matching. In *Advances in Neural Information Processing Systems (NIPS)*, 2019. [3](#)
- [23] Laurent Dinh, David Krueger, and Yoshua Bengio. NICE: non-linear independent components estimation. In *Proc. of the International Conf. on Learning Representations (ICLR)*, 2015. [2](#)

- [24] Laurent Dinh, Jascha Sohl-Dickstein, and Samy Bengio. Density estimation using real NVP. In *Proc. of the International Conf. on Learning Representations (ICLR)*, 2017. 4, 5, 13, 18
- [25] Simon Donne and Andreas Geiger. Learning non-volumetric depth fusion using successive reprojections. In *Proc. IEEE Conf. on Computer Vision and Pattern Recognition (CVPR)*, 2019. 2
- [26] Anastasia Dubrovina, Fei Xia, Panos Achlioptas, Mira Shah, Raphaël Groskot, and Leonidas J. Guibas. Composite shape modeling via latent space factorization. In *Proc. of the IEEE International Conf. on Computer Vision (ICCV)*, pages 8139–8148. IEEE, 2019. 3
- [27] Kevin Ellis, Daniel Ritchie, Armando Solar-Lezama, and Joshua B. Tenenbaum. Learning to infer graphics programs from hand-drawn images. In *Advances in Neural Information Processing Systems (NIPS)*, 2018. 3
- [28] Haoqiang Fan, Hao Su, and Leonidas J. Guibas. A point set generation network for 3d object reconstruction from a single image. *Proc. IEEE Conf. on Computer Vision and Pattern Recognition (CVPR)*, 2017. 1, 2
- [29] Matheus Gadelha, Giorgio Gori, Duygu Ceylan, Radomír Mech, Nathan Carr, Tamy Boubekeur, Rui Wang, and Subhransu Maji. Learning generative models of shape handles. In *Proc. IEEE Conf. on Computer Vision and Pattern Recognition (CVPR)*, 2020. 3
- [30] Matheus Gadelha, Subhransu Maji, and Rui Wang. 3d shape induction from 2d views of multiple objects. In *Proc. of the International Conf. on 3D Vision (3DV)*, 2017. 1, 2
- [31] Jun Gao, Wenzheng Chen, Tommy Xiang, Alec Jacobson, Morgan McGuire, and Sanja Fidler. Learning deformable tetrahedral meshes for 3d reconstruction. In *Advances in Neural Information Processing Systems (NIPS)*, 2020. 2
- [32] Lin Gao, Jie Yang, Tong Wu, Yu-Jie Yuan, Hongbo Fu, Yu-Kun Lai, and Hao Zhang. SDM-NET: deep generative network for structured deformable mesh. In *ACM SIGGRAPH Conference and Exhibition on Computer Graphics and Interactive Techniques in Asia (SIGGRAPH Asia)*, 2019. 3
- [33] Kyle Genova, Forrester Cole, Avneesh Sud, Aaron Sarna, and Thomas A. Funkhouser. Local deep implicit functions for 3d shape. In *Proc. IEEE Conf. on Computer Vision and Pattern Recognition (CVPR)*, 2020. 2, 3
- [34] Kyle Genova, Forrester Cole, Daniel Vlasic, Aaron Sarna, William T Freeman, and Thomas Funkhouser. Learning shape templates with structured implicit functions. In *Proc. of the IEEE International Conf. on Computer Vision (ICCV)*, 2019. 1, 3
- [35] Georgia Gkioxari, Jitendra Malik, and Justin Johnson. Mesh R-CNN. In *Proc. of the IEEE International Conf. on Computer Vision (ICCV)*, 2019. 2
- [36] Amos Gropp, Lior Yariv, Niv Haim, Matan Atzmon, and Yaron Lipman. Implicit geometric regularization for learning shapes. In *Proc. of the International Conf. on Machine Learning (ICML)*, 2020. 2
- [37] Thibault Groueix, Matthew Fisher, Vladimir G. Kim, Bryan C. Russell, and Mathieu Aubry. AtlasNet: A papier-mâché approach to learning 3d surface generation. In *Proc. IEEE Conf. on Computer Vision and Pattern Recognition (CVPR)*, 2018. 1, 2, 3, 17
- [38] Kunal Gupta and Manmohan Chandraker. Neural mesh flow: 3d manifold mesh generation via diffeomorphic flows. *arXiv.org*, 2020. 3
- [39] Christian Häne, Shubham Tulsiani, and Jitendra Malik. Hierarchical surface prediction for 3d object reconstruction. *arXiv.org*, 1704.00710, 2017. 2
- [40] Zekun Hao, Hadar Averbuch-Elor, Noah Snavely, and Serge J. Belongie. Dualsdf: Semantic shape manipulation using a two-level representation. In *Proc. IEEE Conf. on Computer Vision and Pattern Recognition (CVPR)*, 2020. 2
- [41] Wilfried Hartmann, Silvano Galliani, Michal Havlena, Luc Van Gool, and Konrad Schindler. Learned multi-patch similarity. In *Proc. of the IEEE International Conf. on Computer Vision (ICCV)*, 2017. 2
- [42] Kaiming He, Xiangyu Zhang, Shaoqing Ren, and Jian Sun. Deep residual learning for image recognition. In *Proc. IEEE Conf. on Computer Vision and Pattern Recognition (CVPR)*, 2016. 4, 13, 16
- [43] Chiyu Jiang, Avneesh Sud, Ameesh Makadia, Jingwei Huang, Matthias Nießner, and Thomas Funkhouser. Local implicit grid representations for 3d scenes. In *Proc. IEEE Conf. on Computer Vision and Pattern Recognition (CVPR)*, 2020. 2
- [44] Li Jiang, Shaoshuai Shi, Xiaojuan Qi, and Jiaya Jia. GAL: geometric adversarial loss for single-view 3d-object reconstruction. In *Proc. of the European Conf. on Computer Vision (ECCV)*, 2018. 1, 2
- [45] Angjoo Kanazawa, Shubham Tulsiani, Alexei A. Efros, and Jitendra Malik. Learning category-specific mesh reconstruction from image collections. In *Proc. of the European Conf. on Computer Vision (ECCV)*, 2018. 1, 2
- [46] Abhishek Kar, Christian Häne, and Jitendra Malik. Learning a multi-view stereo machine. In *Advances in Neural Information Processing Systems (NIPS)*, 2017. 2
- [47] Yuki Kawana, Yusuke Mukuta, and Tatsuya Harada. Neural star domain as primitive representation. In *Advances in Neural Information Processing Systems (NIPS)*, 2020. 3
- [48] Diederik P. Kingma and Jimmy Ba. Adam: A method for stochastic optimization. In *Proc. of the International Conf. on Learning Representations (ICLR)*, 2015. 14
- [49] Jun Li, Kai Xu, Siddhartha Chaudhuri, Ersin Yumer, Hao (Richard) Zhang, and Leonidas J. Guibas. GRASS: generative recursive autoencoders for shape structures. *ACM Trans. on Graphics*, 36(4), 2017. 3
- [50] Lingxiao Li, Minhyuk Sung, Anastasia Dubrovina, Li Yi, and Leonidas Guibas. Supervised fitting of geometric primitives to 3d point clouds. In *Proc. IEEE Conf. on Computer Vision and Pattern Recognition (CVPR)*, 2019. 3
- [51] Yichen Li, Kaichun Mo, Lin Shao, Minhyuk Sung, and Leonidas J. Guibas. Learning 3d part assembly from a single image. In *Proc. of the European Conf. on Computer Vision (ECCV)*, 2020. 3
- [52] Yiyi Liao, Simon Donne, and Andreas Geiger. Deep marching cubes: Learning explicit surface representations. In *Proc. IEEE Conf. on Computer Vision and Pattern Recognition (CVPR)*, 2018. 1, 2

- [53] Yunchao Liu, Zheng Wu, Daniel Ritchie, William T Freeman, Joshua B Tenenbaum, and Jiajun Wu. Learning to describe scenes with programs. In *Proc. of the International Conf. on Learning Representations (ICLR)*, 2019. 3
- [54] Matthew Loper, Naureen Mahmood, Javier Romero, Gerard Pons-Moll, and Michael J. Black. SMPL: A skinned multi-person linear model. *ACM Trans. on Graphics*, 2015. 33
- [55] Qianli Ma, Shunsuke Saito, Jinlong Yang, Siyu Tang, and Michael J. Black. SCALE: Modeling clothed humans with a surface codec of articulated local elements. In *Proc. IEEE Conf. on Computer Vision and Pattern Recognition (CVPR)*, 2021. 2
- [56] Daniel Maturana and Sebastian Scherer. Voxnet: A 3d convolutional neural network for real-time object recognition. In *Proc. IEEE International Conf. on Intelligent Robots and Systems (IROS)*, 2015. 2
- [57] Lars Mescheder, Michael Oechsle, Michael Niemeyer, Sebastian Nowozin, and Andreas Geiger. Occupancy networks: Learning 3d reconstruction in function space. In *Proc. IEEE Conf. on Computer Vision and Pattern Recognition (CVPR)*, 2019. 1, 2, 3, 7, 16, 24, 27, 28, 29, 30, 31
- [58] Mateusz Michalkiewicz, Jhony K Pontes, Dominic Jack, Mahsa Baktashmotlagh, and Anders Eriksson. Implicit surface representations as layers in neural networks. In *Proc. of the IEEE International Conf. on Computer Vision (ICCV)*, 2019. 1, 2
- [59] Kaichun Mo, Paul Guerrero, Li Yi, Hao Su, Peter Wonka, Niloy Mitra, and Leonidas Guibas. StructureNet: Hierarchical graph networks for 3d shape generation. In *ACM Trans. on Graphics*, 2019. 3
- [60] Michael Niemeyer, Lars Mescheder, Michael Oechsle, and Andreas Geiger. Occupancy flow: 4d reconstruction by learning particle dynamics. In *Proc. of the IEEE International Conf. on Computer Vision (ICCV)*, 2019. 2
- [61] Michael Niemeyer, Lars Mescheder, Michael Oechsle, and Andreas Geiger. Differentiable volumetric rendering: Learning implicit 3d representations without 3d supervision. In *Proc. IEEE Conf. on Computer Vision and Pattern Recognition (CVPR)*, 2020. 2
- [62] Chengjie Niu, Jun Li, and Kai Xu. Im2struct: Recovering 3d shape structure from a single RGB image. In *Proc. IEEE Conf. on Computer Vision and Pattern Recognition (CVPR)*, 2018. 2, 3
- [63] Michael Oechsle, Lars Mescheder, Michael Niemeyer, Thilo Strauss, and Andreas Geiger. Texture fields: Learning texture representations in function space. In *Proc. of the IEEE International Conf. on Computer Vision (ICCV)*, 2019. 2
- [64] Michael Oechsle, Michael Niemeyer, Christian Reiser, Lars Mescheder, Thilo Strauss, and Andreas Geiger. Learning implicit surface light fields. In *Proc. of the International Conf. on 3D Vision (3DV)*, 2020. 2
- [65] Junyi Pan, Xiaoguang Han, Weikai Chen, Jiapeng Tang, and Kui Jia. Deep mesh reconstruction from single RGB images via topology modification networks. In *Proc. of the IEEE International Conf. on Computer Vision (ICCV)*, 2019. 1, 2
- [66] Jeong Joon Park, Peter Florence, Julian Straub, Richard A. Newcombe, and Steven Lovegrove. DeepSDF: Learning continuous signed distance functions for shape representation. In *Proc. IEEE Conf. on Computer Vision and Pattern Recognition (CVPR)*, 2019. 1, 2
- [67] Despoina Paschalidou, Ali Osman Ulusoy, and Andreas Geiger. Superquadrics revisited: Learning 3d shape parsing beyond cuboids. In *Proc. IEEE Conf. on Computer Vision and Pattern Recognition (CVPR)*, 2019. 1, 2, 3, 7, 15, 16, 24
- [68] Despoina Paschalidou, Ali Osman Ulusoy, Carolin Schmitt, Luc van Gool, and Andreas Geiger. Raynet: Learning volumetric 3d reconstruction with ray potentials. In *Proc. IEEE Conf. on Computer Vision and Pattern Recognition (CVPR)*, 2018. 2
- [69] Despoina Paschalidou, Luc van Gool, and Andreas Geiger. Learning unsupervised hierarchical part decomposition of 3d objects from a single rgb image. In *Proc. IEEE Conf. on Computer Vision and Pattern Recognition (CVPR)*, 2020. 1, 2, 3, 7, 16, 24
- [70] Adam Paszke, Abhishek Chaurasia, Sangpil Kim, and Eugenio Culurciello. Enet: A deep neural network architecture for real-time semantic segmentation. *arXiv.org*, 1606.02147, 2016. 16
- [71] Georgios Pavlakos, Vasileios Choutas, Nima Ghorbani, Timo Bolkart, Ahmed A. A. Osman, Dimitrios Tzionas, and Michael J. Black. Expressive body capture: 3d hands, face, and body from a single image. In *Proc. IEEE Conf. on Computer Vision and Pattern Recognition (CVPR)*, 2019. 8, 33
- [72] Songyou Peng, Michael Niemeyer, Lars Mescheder, Marc Pollefeys, and Andreas Geiger. Convolutional occupancy networks. In *Proc. of the European Conf. on Computer Vision (ECCV)*, 2020. 2
- [73] Charles R Qi, Li Yi, Hao Su, and Leonidas J Guibas. PointNet++: Deep hierarchical feature learning on point sets in a metric space. In *Advances in Neural Information Processing Systems (NIPS)*, 2017. 1, 2
- [74] Edoardo Remelli, Artem Lukoianov, Stephan R. Richter, Benoît Guillard, Timur M. Bagautdinov, Pierre Baqué, and Pascal Fua. MeshSDF: Differentiable iso-surface extraction. 2020. 2
- [75] Danilo Jimenez Rezende, S. M. Ali Eslami, Shakir Mohamed, Peter Battaglia, Max Jaderberg, and Nicolas Heess. Unsupervised learning of 3d structure from images. In *Advances in Neural Information Processing Systems (NIPS)*, 2016. 1, 2
- [76] Gernot Riegler, Ali Osman Ulusoy, Horst Bischof, and Andreas Geiger. OctNetFusion: Learning depth fusion from data. In *Proc. of the International Conf. on 3D Vision (3DV)*, 2017. 2
- [77] Gernot Riegler, Ali Osman Ulusoy, and Andreas Geiger. Octnet: Learning deep 3d representations at high resolutions. In *Proc. IEEE Conf. on Computer Vision and Pattern Recognition (CVPR)*, 2017. 1, 2
- [78] Lawrence G. Roberts. *Machine perception of three-dimensional solids*. PhD thesis, Massachusetts Institute of Technology, 1963. 2
- [79] Javier Romero, Dimitrios Tzionas, and Michael J. Black. Embodied hands: modeling and capturing hands and bodies together. *ACM Trans. Gr.*, 36(6):245:1–245:17, 2017. 7, 26

- [80] Shunsuke Saito, Zeng Huang, Ryota Natsume, Shigeo Morishima, Angjoo Kanazawa, and Hao Li. Pifu: Pixel-aligned implicit function for high-resolution clothed human digitization. In *Proc. of the IEEE International Conf. on Computer Vision (ICCV)*, 2019. 1, 2
- [81] Shunsuke Saito, Tomas Simon, Jason M. Saragih, and Hanbyul Joo. Pifuhd: Multi-level pixel-aligned implicit function for high-resolution 3d human digitization. In *Proc. IEEE Conf. on Computer Vision and Pattern Recognition (CVPR)*, 2020. 2
- [82] Gopal Sharma, Rishabh Goyal, Difan Liu, Evangelos Kalogerakis, and Subhransu Maji. Csgnet: Neural shape parser for constructive solid geometry. In *Proc. IEEE Conf. on Computer Vision and Pattern Recognition (CVPR)*, 2018. 3
- [83] Gopal Sharma, Difan Liu, Subhransu Maji, Evangelos Kalogerakis, Siddhartha Chaudhuri, and Radomír Mech. Parsenet: A parametric surface fitting network for 3d point clouds. In Andrea Vedaldi, Horst Bischof, Thomas Brox, and Jan-Michael Frahm, editors, *Proc. of the European Conf. on Computer Vision (ECCV)*, 2020. 3
- [84] David Stutz and Andreas Geiger. Learning 3d shape completion from laser scan data with weak supervision. In *Proc. IEEE Conf. on Computer Vision and Pattern Recognition (CVPR)*, 2018. 1, 2, 27
- [85] Towaki Takikawa, Joey Litalien, Kangxue Yin, Karsten Kreis, Charles Loop, Derek Nowrouzezahrai, Alec Jacobson, Morgan McGuire, and Sanja Fidler. Neural geometric level of detail: Real-time rendering with implicit 3D shapes. *arXiv preprint arXiv:2101.10994*, 2021. 2
- [86] M. Tatarchenko, A. Dosovitskiy, and T. Brox. Octree generating networks: Efficient convolutional architectures for high-resolution 3d outputs. In *Proc. of the IEEE International Conf. on Computer Vision (ICCV)*, 2017. 2
- [87] Hugues Thomas, Charles R. Qi, Jean-Emmanuel Deschaud, Beatriz MarcoteGUI, François Goulette, and Leonidas J. Guibas. Kpconv: Flexible and deformable convolution for point clouds. In *Proc. of the IEEE International Conf. on Computer Vision (ICCV)*, 2019. 1, 2
- [88] Yonglong Tian, Andrew Luo, Xingyuan Sun, Kevin Ellis, William T Freeman, Joshua B Tenenbaum, and Jiajun Wu. Learning to infer and execute 3d shape programs. In *Proc. of the International Conf. on Learning Representations (ICLR)*, 2019. 3
- [89] Shubham Tulsiani, Nilesh Kulkarni, and Abhinav Gupta. Implicit mesh reconstruction from unannotated image collections. *arXiv.org*, 2020. 3
- [90] Shubham Tulsiani, Hao Su, Leonidas J. Guibas, Alexei A. Efros, and Jitendra Malik. Learning shape abstractions by assembling volumetric primitives. In *Proc. IEEE Conf. on Computer Vision and Pattern Recognition (CVPR)*, 2017. 1, 2, 3
- [91] Nanyang Wang, Yinda Zhang, Zhuwen Li, Yanwei Fu, Wei Liu, and Yu-Gang Jiang. Pixel2mesh: Generating 3d mesh models from single rgb images. In *Proc. of the European Conf. on Computer Vision (ECCV)*, 2018. 1, 2, 3
- [92] WeiyueXu Wang, Qiangeng Xu, Duygu Ceylan, Radomir Mech, and Ulrich Neumann. Disn: Deep implicit surface network for high-quality single-view 3d reconstruction. In *Advances in Neural Information Processing Systems (NIPS)*, 2019. 2
- [93] Jiajun Wu, Chengkai Zhang, Tianfan Xue, Bill Freeman, and Josh Tenenbaum. Learning a probabilistic latent space of object shapes via 3d generative-adversarial modeling. In *Advances in Neural Information Processing Systems (NIPS)*, 2016. 2
- [94] Haozhe Xie, Hongxun Yao, Xiaoshuai Sun, Shangchen Zhou, and Shengping Zhang. Pix2vox: Context-aware 3d reconstruction from single and multi-view images. In *Proc. of the IEEE International Conf. on Computer Vision (ICCV)*, 2019. 1, 2
- [95] Qiangeng Xu, Weiyue Wang, Duygu Ceylan, Radomír Mech, and Ulrich Neumann. DISN: deep implicit surface network for high-quality single-view 3d reconstruction. In *Advances in Neural Information Processing Systems (NIPS)*, 2019. 1, 2
- [96] Guandao Yang, Xun Huang, Zekun Hao, Ming-Yu Liu, Serge J. Belongie, and Bharath Hariharan. Pointflow: 3d point cloud generation with continuous normalizing flows. In *Proc. of the IEEE International Conf. on Computer Vision (ICCV)*, 2019. 1, 2
- [97] Xiuming Zhang, Sean Ryan Fanello, Yun-Ta Tsai, Tiancheng Sun, Tianfan Xue, Rohit Pandey, Sergio Orts-Escolano, Philip L. Davidson, Christoph Rhemann, Paul E. Debevec, Jonathan T. Barron, Ravi Ramamoorthi, and William T. Freeman. Neural light transport for relighting and view synthesis. *arXiv.org*, 2008.03806, 2020. 2
- [98] Christian Zimmermann, Duygu Ceylan, Jimei Yang, Bryan Russell, Max Argus, and Thomas Brox. Freihand: A dataset for markerless capture of hand pose and shape from single rgb images. In *Proc. of the IEEE International Conf. on Computer Vision (ICCV)*, 2019. 2, 7, 13, 26
- [99] Chuhang Zou, Ersin Yumer, Jimei Yang, Duygu Ceylan, and Derek Hoiem. 3d-prnn: Generating shape primitives with recurrent neural networks. In *Proc. of the IEEE International Conf. on Computer Vision (ICCV)*, 2017. 2, 3

# Supplementary Material for Neural Parts: Learning Expressive 3D Shape Abstractions with Invertible Neural Networks

Despoina Paschalidou<sup>1,5,6</sup> Angelos Katharopoulos<sup>3,4</sup> Andreas Geiger<sup>1,2,5</sup> Sanja Fidler<sup>6,7,8</sup>

<sup>1</sup>Max Planck Institute for Intelligent Systems Tübingen <sup>2</sup>University of Tübingen

<sup>3</sup>Idiap Research Institute, Switzerland <sup>4</sup>École Polytechnique Fédérale de Lausanne (EPFL)

<sup>5</sup>Max Planck ETH Center for Learning Systems <sup>6</sup>NVIDIA <sup>7</sup>University of Toronto <sup>8</sup>Vector Institute

{firstname.lastname}@tue.mpg.de angelos.katharopoulos@idiap.ch sfidler@nvidia.com

## Abstract

In this *supplementary document*, we first present a detailed overview of our network architecture and the training procedure. We then provide ablations on how different components of our system impact the performance of our model on the single-view 3D reconstruction task. Subsequently, we provide additional experimental results on the D-FAUST [8], the FreiHAND [98] and ShapeNet [10] dataset. Next, we provide additional evidence for the representation consistency of our method.

## A. Implementation Details

In this section, we provide a detailed description of our network architecture. We then describe our training protocol, our sampling strategy and provide details on the computation of the metrics during training and testing. Finally, we also provide additional details regarding our baselines.

### A.1. Network Architecture

Here we describe the architecture of each individual component of our model (from Fig. 2 in main submission). Our architecture comprises two main components: (i) a *feature extractor* that maps the input into a vector of per-primitive shape embeddings  $\{\mathbf{C}_m\}_{m=1}^M$  and (ii) the *conditional homeomorphism* that learns a family of homeomorphic mappings between the sphere and the target shape, conditioned on the shape embedding.

**Feature Extractor:** The first part of the *feature extractor* is the feature encoder. In our experiments, the feature encoder is implemented with a ResNet-18 architecture [42] that is pre-trained on ImageNet [20]. From the original architecture, we remove the final fully connected layer and keep only the feature vector of length 512 after average pooling. Subsequently, we use 2 fully connected layers to map this to the global feature vector  $\mathbf{F} \in \mathbb{R}^{256}$ . During training, we use the pre-trained batch statistics for normalization. The primitive embedding  $\{\mathbf{P}_m\}_{m=1}^M$  is a matrix of size  $M \times 256$ , that stores a vector per-primitive index that is concatenated with the global image feature  $\mathbf{F}$  and outputs a vector of shape embeddings  $\{\mathbf{C}_m \in \mathbb{R}^{512}\}_{m=1}^M$  for every primitive. A pictorial representation of the feature extractor is provided in Fig. 11.

**Conditional Homeomorphism:** The conditional homeomorphism is implemented with a Real NVP [24] augmented as described in the main submission. It comprises 4 coupling layers and each coupling layer consists of three components:  $s_\theta(\cdot)$  that predicts the **scaling factor**  $s$ ,  $t_\theta(\cdot)$  that predicts the **translation amount**  $t$  and  $p_\theta(\cdot)$  that maps the input 3D point to a higher dimensional space before concatenating it with the per-primitive shape embedding  $\mathbf{C}_m$ . In particular,  $s_\theta(\cdot)$  is a 3-layer MLP with hidden size equal to 256. After each layer we add ReLU non-linearities except for the last layer, where we use a hard tanh with thresholds  $-10$  and  $10$  (see Fig. 12a). Note that we use the tanh to avoid numerical instabilities when computing the exponential of the scaling factor.  $t_\theta(\cdot)$  is implemented with the same architecture apart from the tanh activation in the final layer (see Fig. 12b). Finally,  $p_\theta(\cdot)$  is implemented with a 2-layer MLP with ReLU non-linearities with hidden size 256 and output size 128. An illustration of the components of the conditional homeomorphism is provided in

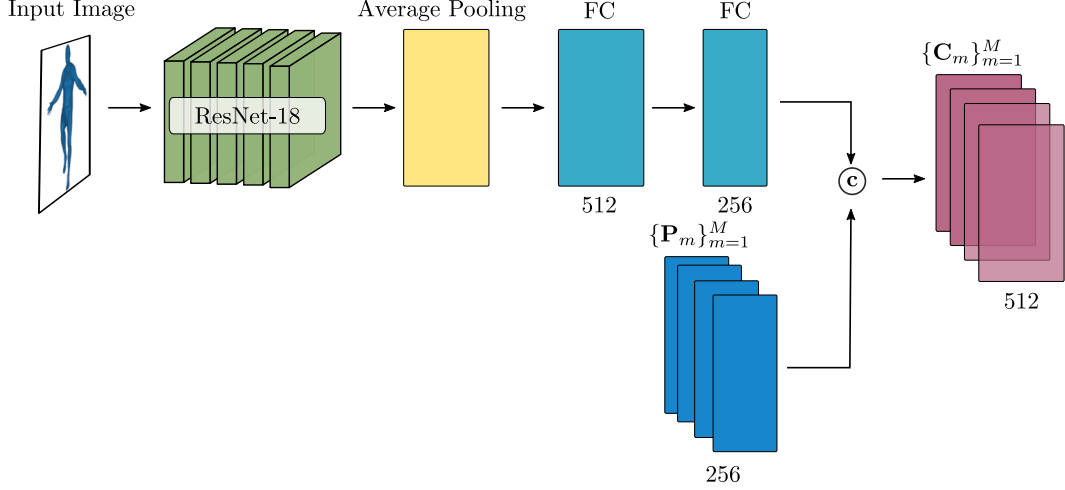


Figure 11: **Feature Extractor.** The feature extractor predicts a vector of per-primitive shape embeddings  $\{C_m\}_{m=1}^M$  conditioned on the input image. Note that depending on the type of the input (e.g. pointcloud, voxel grid), a different feature encoder module needs to be employed.

Fig. 12. As discussed in the main submission, we split the dimensions of the input point  $(x_i, y_i, z_i)$  in order to scale and

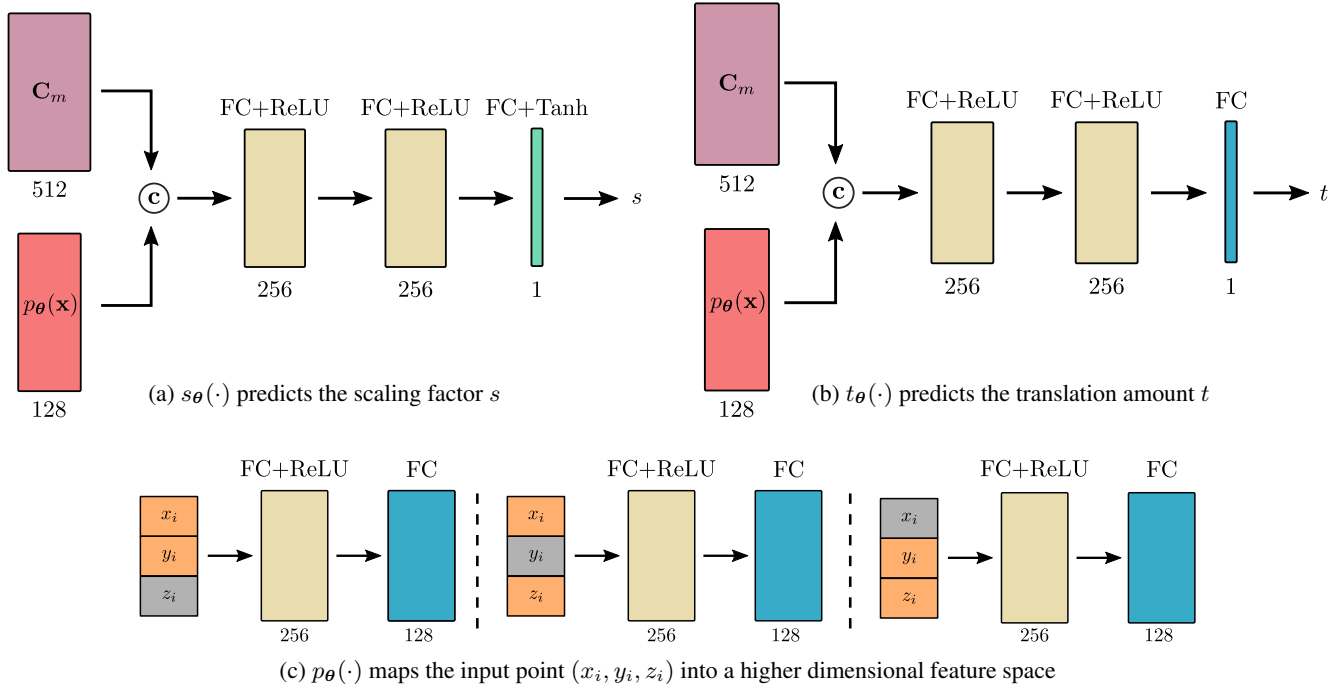


Figure 12: **Conditional Homeomorphism.** The conditional homeomorphism is the backbone of our architecture that given a vector of per-primitive shape embeddings and a set of points on the sphere in the latent space maps them in the primitive space of the target object and vice versa. Here, we visualize  $s_{\theta}(\cdot)$ ,  $t_{\theta}(\cdot)$  and  $p_{\theta}(\cdot)$  that comprise our *affine coupling layer*.

translate one of them based on the other two. In practice, this is efficiently implemented via masking one of the dimensions, as illustrated in Fig. 12c with gray.

## A.2. Training Protocol

In all our experiments, we use the Adam optimizer [48] with learning rate  $\eta = 10^{-4}$  and no weight decay. For the other hyperparameters of Adam we use the PyTorch defaults. Depending on the number of primitives, we train our model with

a different batch size and a different number of iterations. In particular, for 2 primitives, we use a batch size of 6 for 100k iterations and we aggregate the gradients over 2 batches. For the experiments, with 5 primitives, we use a batch size of 4 for 150k iterations and we again aggregate the gradients over 2 batches. For 8 and 10 primitives, we use a batch size of 4 for 200k iterations and aggregate the gradients over 4 batches. We do not perform any data augmentation.

We weigh the loss terms of Eq. 11 in our main submission with 1.0, 0.1, 0.01, 0.1, 0.01. Note that we use smaller weights for  $\mathcal{L}_{norm}$  and  $\mathcal{L}_{cover}$  since they act as regularizers and we want our model to focus primarily on learning geometrically accurate and semantically meaningful primitives. The impact of each term is discussed in detail in Sec. B.3. The temperature parameter  $\tau$  in the occupancy  $\mathcal{L}_{occ}$  and the overlap loss  $\mathcal{L}_{overlap}$  is set to  $4 \times 10^{-3}$ . In addition, the  $k$  term for the  $\mathcal{L}_{overlap}$  is set to 1.95 since we want to penalize overlapping primitives but ensure that they will be connected. Note that  $k = 1$  results in disconnected primitives and  $k = 2$  allows primitives to overlap in pairs of two. Hence we select  $k = 1.95$  as we empirically observe that it balances connectivity and interpenetration. Finally, we set the  $k$  to be equal to 10 for the  $\mathcal{L}_{cover}$ , as we empirically observe that it leads to good performance.

### A.3. Sampling Strategy

In this section, we discuss our sampling strategy for generating the surface samples  $\mathcal{X}_t = \{\mathbf{x}_i, \mathbf{n}_i\}_{i=1}^N$ , the occupancy pairs  $\mathcal{X}_o = \{\mathbf{x}_i, o_i\}_{i=1}^V$  and the points on the sphere surface  $\mathcal{Y}_s = \{\mathbf{y}_j\}_{j=1}^K$ .

**Surface Samples:** We generate samples on the surface of the target mesh by sampling a face with probability proportional to its area and then sampling a point uniformly in that face. We use the corresponding face normals to generate point-normal pairs from the target mesh. During training, we randomly sample 2,000 points and normals on the target mesh.

**Occupancy Pairs:** We generate occupancy pairs by sampling 100,000 points uniformly in the unit cube centered at  $(0, 0, 0)$  for each mesh. Subsequently, we compute which of these points lie inside or outside the mesh to generate the occupancy labels. However, because the target objects have a small volume compared to the unit cube, resampling uniformly from the 100,000 occupancy pairs results in a small amount of points with positive labels. This yields bad reconstructions for parts with small volume such as hands and fingers. To address this, we sample from an unbalanced distribution that, in expectation, results in an equal number of points with positive and negative labels. However, we also compute importance sampling weights in order to reweigh our loss and create an unbiased estimator of the loss with uniform sampling similar to [67]. During training, we sample 5,000 occupancy pairs.

**Sphere Points:** In order to generate points on the surface of each primitive, we sample points uniformly on the surface of a sphere with radius  $r$  by sampling points from a 3-D isotropic Gaussian and normalizing their length to  $r$ . Note that this does not generate uniform samples on the surface of the primitive due to different amounts of stretching and contracting of the sphere by each homeomorphism. However, we empirically observe that this sampling does not impact negatively the training of our model, thus we leave sampling uniformly on the surface of each primitive for future work. During training we sample 200 points for each primitive. In addition, to generate meshes for the predicted primitives, we also need to compute sphere surface points and corresponding faces. We achieve this using the  $UV$  parametrization of the sphere [17]. For visualization purposes we use 2,000 points sampled uniformly in latitude and longitude.

### A.4. Metrics

As mentioned in the main submission, we evaluate our model and our baselines using the volumetric Intersection-over-Union (IoU) and the Chamfer- $L_1$  distance. We obtain unbiased low-variance estimates for the IoU by sampling 100,000 points from the bounding volume and determining if the points lie inside or outside the target/predicted mesh. Similarly, we obtain an unbiased low-variance estimator of the Chamfer- $L_1$  distance by sampling 10,000 points on the surface of the target/predicted mesh.

Volumetric IoU is defined as the quotient of the volume of the intersection of the target  $O_t$  and the predicted  $O_p$  object and the volume of their union.

$$\text{IoU}(O_t, O_p) = \frac{|V(O_t \cap O_p)|}{|V(O_t \cup O_p)|} \quad (17)$$

where  $V(\cdot)$  is a function that computes the volume of a mesh.

The Chamfer- $L_1$  distance is defined between a set of points sampled on the surface of the target and the predicted mesh. We denote  $\mathcal{X} = \{\mathbf{x}_i\}_{i=1}^N$  the set of points sampled on the surface of the target mesh and  $\mathcal{Y} = \{\mathbf{y}_i\}_{i=1}^M$  the set of points

sampled on the surface of the predicted mesh.

$$\text{Chamfer-}L_1(\mathcal{X}, \mathcal{Y}) = \frac{1}{N} \sum_{\mathbf{x} \in \mathcal{X}} \min_{\mathbf{y} \in \mathcal{Y}} \|\mathbf{x} - \mathbf{y}\| + \frac{1}{M} \sum_{\mathbf{y} \in \mathcal{Y}} \min_{\mathbf{x} \in \mathcal{X}} \|\mathbf{y} - \mathbf{x}\| \quad (18)$$

The first term of (18) measures the *completeness* of the predicted shape, namely how far is on average the closest predicted point from a ground-truth point. The second term measures the *accuracy* of the predicted shape, namely how far on average is the closest ground-truth point from a predicted point. Note that during the evaluation we do not sample points on the sphere to generate points on the surface of the primitives. Instead we use the predicted meshes to ensure that the generated points are uniformly distributed on the surface of the predicted object.

## A.5. Baselines

In this section, we provide additional details regarding our baselines. For a fair comparison, all baselines use the same feature extractor network, namely ResNet18 [42].

**SQs:** In SQs [67], the authors employ a convolutional neural network (CNN) to regress the parameters of a set of superquadric surfaces that best describe the target object, in an unsupervised manner, by minimizing the Chamfer-distance between points on the target and the predicted shape. In order to have predictions, with variable number of primitives, each primitive is associated with an existence probability. When the existence probability of a primitive is below a threshold this primitive is not part of the assembled object. We train SQs [67]<sup>2</sup> using the provided PyTorch [70] implementation with the default parameters. Similar to our model, we sample 200 points on the surface of each primitive and 2,000 on the surface of the target object. We train SQs with a batch size of 32 until convergence.

**H-SQs:** H-SQs [69] consider a hierarchical, geometrically more accurate decomposition of parts using superquadrics. In particular, H-SQs employ a neural network architecture that recursively partitions objects into their constituent parts by building a latent vector that jointly encodes both the part-level hierarchy and the part geometries. H-SQs are trained in an unsupervised fashion, with an occupancy loss function such that the model learns to classify whether points sampled in the bounding box that contains the target object lie inside or outside the union of the predicted primitives. We train H-SQs [69] using the PyTorch code provided by the authors. Note that the maximum number of primitives for H-SQs needs to be a power of 2, hence we train with a different number of primitives than the other baselines. Again, we train H-SQs with a batch size of 32 until convergence.

**CvxNet:** CvxNet [19] propose to reconstruct a 3D shape as a collection of convex hulls. We train CvxNet [19]<sup>3</sup> using the provided TensorFlow [1] code with the default parameters. To ensure that the evaluation is consistent and fair, we extract meshes using their codebase and evaluate the predicted primitives using our evaluation code. For all datasets, we train CvxNet with a batch size of 32 until convergence using their default parameters.

**OccNet:** In our evaluation, we also include OccNet [57]<sup>4</sup> which we train using the provided code by the authors. In particular, OccNet is trained with a batch size of 32 until convergence. While OccNet does not consider any part-based decomposition of the target object and is not directly comparable with our model, we include it in our analysis as a typical representative of powerful implicit shape extraction techniques

---

<sup>2</sup><https://superquadrics.com/>

<sup>3</sup><https://cvxnet.github.io/>

<sup>4</sup>[https://github.com/autonomousvision/occupancy\\_networks](https://github.com/autonomousvision/occupancy_networks)

## B. Ablation Study

In this section, we investigate how various components of our system affect the performance of Neural Parts on the single-view 3D reconstruction task on the D-FAUST dataset. In Sec. B.1, we examine the impact of the INN on the performance of our model. Next, in Sec. B.2, we investigate the impact of  $p_\theta(\cdot)$  and in Sec. B.3, we discuss the effect of each loss term on the overall performance of our model. Unless stated otherwise, we train all models with 5 primitives for 300 epochs.

### B.1. Invertibility

In this section, we examine the impact of the Invertible Neural Network (INN) on the performance of Neural Parts. To this end, we implement a variant of our model that does not consider the inverse mapping of the homeomorphism, namely without the  $\phi_\theta^{-1}(\mathbf{x})$ . As a result, for this variant it is not possible to compute the union of parts, as formulated in Eq. 10 in our main submission, namely we cannot discard points on a primitive’s surface that are internal to another primitive when generating points on the surface of the predicted shape. Moreover, we cannot impose any additional constraints on the predicted primitives. Therefore, we train this variant using the reconstruction loss between the target  $\mathcal{X}_t$  and the predicted  $\mathcal{X}_{\hat{p}}$  shape,  $\mathcal{L}_{rec}(\mathcal{X}_t, \mathcal{X}_{\hat{p}})$  from Eq 12 in our main submission as follows:

$$\mathcal{L}_{rec}(\mathcal{X}_t, \mathcal{X}_{\hat{p}}) = \frac{1}{|\mathcal{X}_t|} \sum_{\mathbf{x}_i \in \mathcal{X}_t} \min_{\mathbf{x}_j \in \mathcal{X}_{\hat{p}}} \|\mathbf{x}_i - \mathbf{x}_j\|_2^2 + \frac{1}{|\mathcal{X}_{\hat{p}}|} \sum_{\mathbf{x}_j \in \mathcal{X}_{\hat{p}}} \min_{\mathbf{x}_i \in \mathcal{X}_t} \|\mathbf{x}_i - \mathbf{x}_j\|_2^2 \quad (19)$$

where  $\mathcal{X}_{\hat{p}} = \mathbf{x} \in \bigcup_m \mathcal{X}_p^m$ , namely the union of surface points on each primitive.

Furthermore, we introduce an additional baseline that replaces the INN with an MLP. Similar to AtlasNet [37], we use a 4-layer MLP to learn the homeomorphic mappings between the sphere and the target object. Since the homeomorphism is implemented via an MLP it is not possible to define its inverse mapping. Thus, also this baseline is trained using the loss of (19). Note that this baseline is slightly different from AtlasNet [37] because instead of having a single MLP for each homeomorphism, we have one MLP for the  $M$  homeomorphisms. In particular, for this baseline, we implement the decoder architecture proposed in [37].

	w/o $\phi_\theta^{-1}(\mathbf{x})$	AtlasNet - sphere	Ours
IoU	0.639	*	0.673
Chamfer- $L_1$	0.119	0.087	0.097

Table 1: **Ablation Study on INN.** This table shows a quantitative comparison of our approach wrt. a variant of our model that does not consider the inverse mapping of the homeomorphism and a second baseline that replaces the INN with an MLP for learning the homeomorphic mapping. We refer to the latter as AtlasNet - sphere, as it is a variant of the original AtlasNet method [37]. We note that our model outperforms both baseline both in terms of IoU ( $\uparrow$ ) and Chamfer- $L_1$  distance ( $\downarrow$ ).

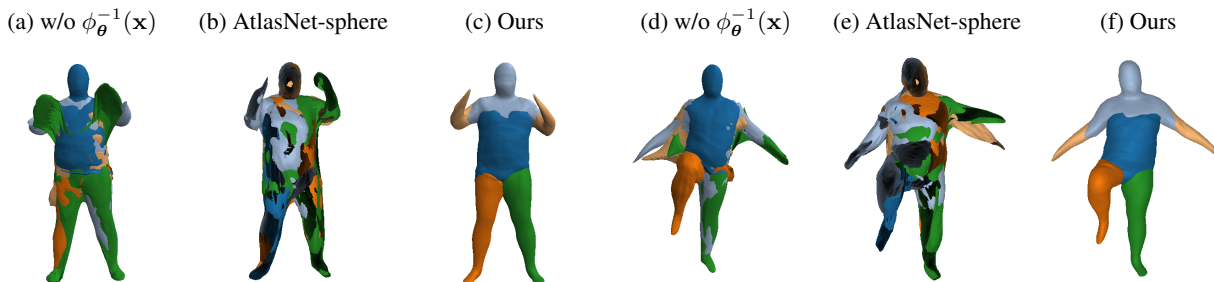


Figure 13: **Qualitative evaluation on the impact of the INN.** We visualize the predicted primitives for our model (third and sixth column), a variant of our model that ignores the inverse mapping of the homeomorphism (first and fourth column) and the AtlasNet-sphere baseline that implements the homeomorphism with an MLP.

Tab. 1 summarizes the quantitative comparison between our model and the aforementioned baselines. Note that for the AtlasNet-sphere baseline, we cannot compute the IoU since it is not possible to enforce that the predicted primitives do

not degenerate to “sheets”, which contain no points (zero volume primitives). Indeed, from our evaluation, we observe that almost all predicted primitives (see Fig. 14) have zero volume and also inverted normals, which means that the sphere has folded on itself (self-intersections). This is only possible if the MLP is not implementing a homeomorphism. Due to the aforementioned issues, the AtlasNet-sphere cannot be used for learning primitives, however, we validate that it achieves high scores in terms of Chamfer- $L_1$  distance, which is justified as AtlasNet-sphere is optimized solely on this metric.

On the contrary, our method always learns valid homeomorphisms even when the inverse mapping ( $\phi_{\theta}^{-1}(\cdot)$ ) is not used during training. This becomes evident from Fig. 13a+Fig. 13d, where we observe that the predicted primitives do not have inverted normals. However, without the inverse mapping we cannot enforce that primitives will not interpenetrate, hence the predicted primitives lack interpretability.



Figure 14: **Predicted primitives of AtlasNet-sphere.** We visualize the individual primitives for the predictions of AtlasNet-sphere in Fig. 9a. Note that some of the predicted primitives are hollow (first, third, sixth and eighth), some have holes (second, seventh) and all of them have inverted normals.

## B.2. Effect of $p_{\theta}(\cdot)$

The original Real NVP [24] cannot be directly applied in our setting as it does not consider a shape embedding. To address this, we augment the affine coupling layer as follows: we first map  $(x_i, y_i)$  into a higher dimensional feature vector using a mapping,  $p_{\theta}(\cdot)$ , implemented as an MLP. This is done to increase the relative importance of the input point before concatenating it with the high-dimensional shape embedding  $C_m$ . The *conditional affine coupling layer* becomes

$$\begin{aligned} x_o &= x_i \\ y_o &= y_i \\ z_o &= z_i \exp(s_{\theta}([C_m; p_{\theta}(x_i, y_i)])) + t_{\theta}([C_m; p_{\theta}(x_i, y_i)]) \end{aligned} \tag{20}$$

where  $[\cdot; \cdot]$  denotes concatenation. A graphical representation of our conditional coupling layer is provided in Fig. 15a. In this section, we examine the impact of the mapping  $p_{\theta}(\cdot)$  on the performance of our model. In particular, instead of first mapping the input point  $(x_i, y_i, z_i)$  into a higher dimensional space and then concatenating it with the per-primitive shape embedding  $C_m$ , we concatenate it as is (see Fig. 15b).

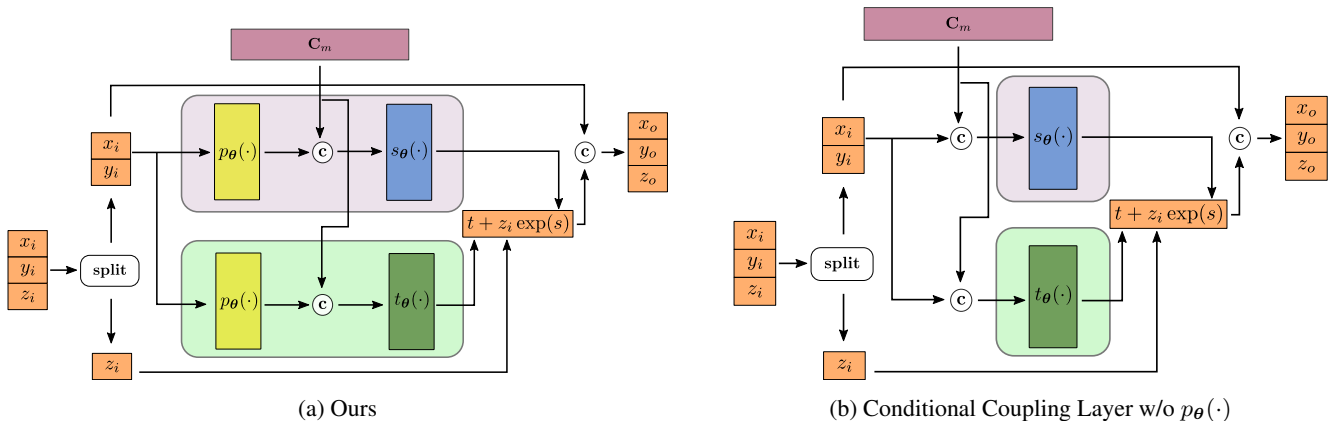


Figure 15: **Conditional Coupling Layer.** Pictorial representation of our conditional affine coupling layer. The input point  $(x_i, y_i, z_i)$  is passed into a *coupling layer* that scales and translates one dimension of the input based on the other two and the per-primitive shape embedding  $C_m$ . The scale factor  $s$  and the translation amount  $t$  are predicted by two MLPs,  $s_{\theta}(\cdot)$  and  $t_{\theta}(\cdot)$ .  $p_{\theta}(\cdot)$  is another MLP that increases the dimensionality of the input point before it is concatenated with  $C_m$ .

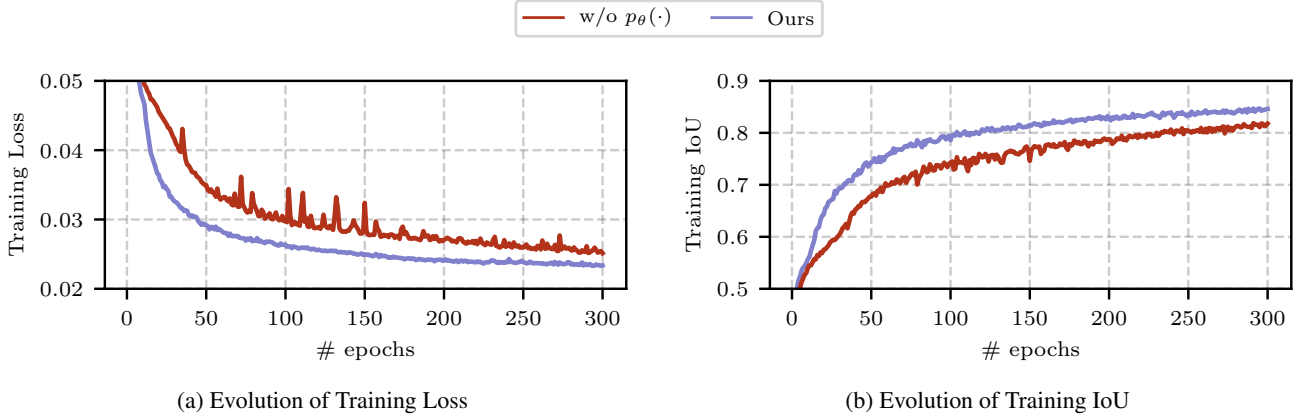


Figure 16: **Training Convergence w/o  $p_{\theta}(\cdot)$ .** We illustrate the training evolution over 300 epochs in terms of training loss (Eq. 11 in the main submission) and IoU for our method with (purple) and without  $p_{\theta}(\cdot)$  (red). We observe that our method converges smoother and to a lower loss and higher IoU when using  $p_{\theta}(\cdot)$ .

We observe that removing  $p_{\theta}(\cdot)$  makes it harder for the network to produce a scaling and translation dependent on the input point due to the large difference in the number of dimensions compared to the shape embedding  $C_m$ . This results in slower convergence in comparison to our full model (see Fig. 16). Moreover, we also notice that the reconstruction quality becomes worse both in terms of IoU and Chamfer- $L_1$  distance (see Tab. 2).

	w/o $p_{\theta}(\cdot)$	Ours
IoU	0.638	0.673
Chamfer- $L_1$	0.106	0.097

Table 2: **Ablation Study on  $p_{\theta}(\cdot)$ .** This table shows a numeric comparison of our approach wrt. a variant of our model that does not utilize  $p_{\theta}(\cdot)$ , namely instead of first mapping the input point  $(x_i, y_i, z_i)$  into a higher dimensional space, we directly concatenate the input point with the per-primitive shape embedding  $C_m$ .

### B.3. Loss Functions

Neural Parts are trained in an unsupervised fashion, without any primitive annotations. To address, the lack of part-level supervision, we learn this task by minimizing the geometric distance between the target and the predicted shape. In particular, our optimization objective comprises of five loss terms that enforce that the predicted primitives are geometrically accurate and semantically meaningful.

$$\mathcal{L} = \mathcal{L}_{rec}(\mathcal{X}_t, \mathcal{X}_p) + \mathcal{L}_{occ}(\mathcal{X}_o) + \mathcal{L}_{norm}(\mathcal{X}_t) + \mathcal{L}_{overlap}(\mathcal{X}_o) + \mathcal{L}_{cover}(\mathcal{X}_o). \quad (21)$$

In this section, we discuss how each loss term affects the performance of our model on the single-view 3D reconstruction task. In particular, we train 5 variants of our model and for each one we omit one of each loss terms. We provide both quantitative (see Tab. 3) and qualitative comparison (see Fig. 17) for the 5 different scenarios. For a fair comparison all models are trained for the same number of epochs.

	w/o $\mathcal{L}_{occ}$	w/o $\mathcal{L}_{rec}$	w/o $\mathcal{L}_{norm}$	w/o $\mathcal{L}_{overlap}$	w/o $\mathcal{L}_{cover}$	Ours
IoU	0.642	0.643	0.669	0.670	0.668	0.673
Chamfer- $L_1$	0.125	0.150	0.096	0.098	0.096	0.097

Table 3: **Ablation Study on Loss Terms.** We investigate the impact of each loss term by training our model without each one of them. We report the IoU ( $\uparrow$ ) and the Chamfer- $L_1$  distance ( $\downarrow$ ) on the single-view 3D reconstruction task on D-FAUST dataset.



Figure 17: **Ablation Study on Loss Terms.** Qualitative evaluation of the impact of the 5 loss terms on the performance of our model. We train Neural Parts, without each loss term and visualize the predicted primitives.

**w/o Reconstruction Loss:** The reconstruction loss is a bidirectional Chamfer loss between the surface points on the target and the predicted shape. We note that removing  $\mathcal{L}_{rec}(\mathcal{X}_t, \mathcal{X}_p)$  results in degenerate primitive arrangements that fail to capture the object geometry.

**w/o Occupancy Loss:** The occupancy loss enforces that the free and the occupied space of the predicted and the target

object will coincide. Therefore, when we remove  $\mathcal{L}_{occ}(\mathcal{X}_o)$  from our optimization objective, we observe that the predicted primitives accurately represent geometric parts of the human body but fail to capture the empty space (see hands and legs in first column of Fig. 17). Note that the points on the primitive surface that capture empty space have a small distance from points on the target object and as a result,  $\mathcal{L}_{rec}(\mathcal{X}_t, \mathcal{X}_p)$  has small values for these points, which makes it difficult to penalize them for covering unoccupied space.

**w/o Normal Consistency Loss:** The normal consistency loss enforces that the normals of the predicted primitives will be aligned with the normals of the target object. We notice that when we remove  $\mathcal{L}_{norm}(\mathcal{X}_t)$ , our model yields non-overlapping primitives that accurately capture the geometry of different human body parts (see Fig. 19). However, at the locations where one primitive meets its adjacent, the predicted primitives have inconsistent normals, hence the connections seem unnatural. This can be better seen in Fig. 18, where we provide close-ups on the locations where two primitives meet and compare with our model. Our model, yields primitives with smooth transitions that look more natural.

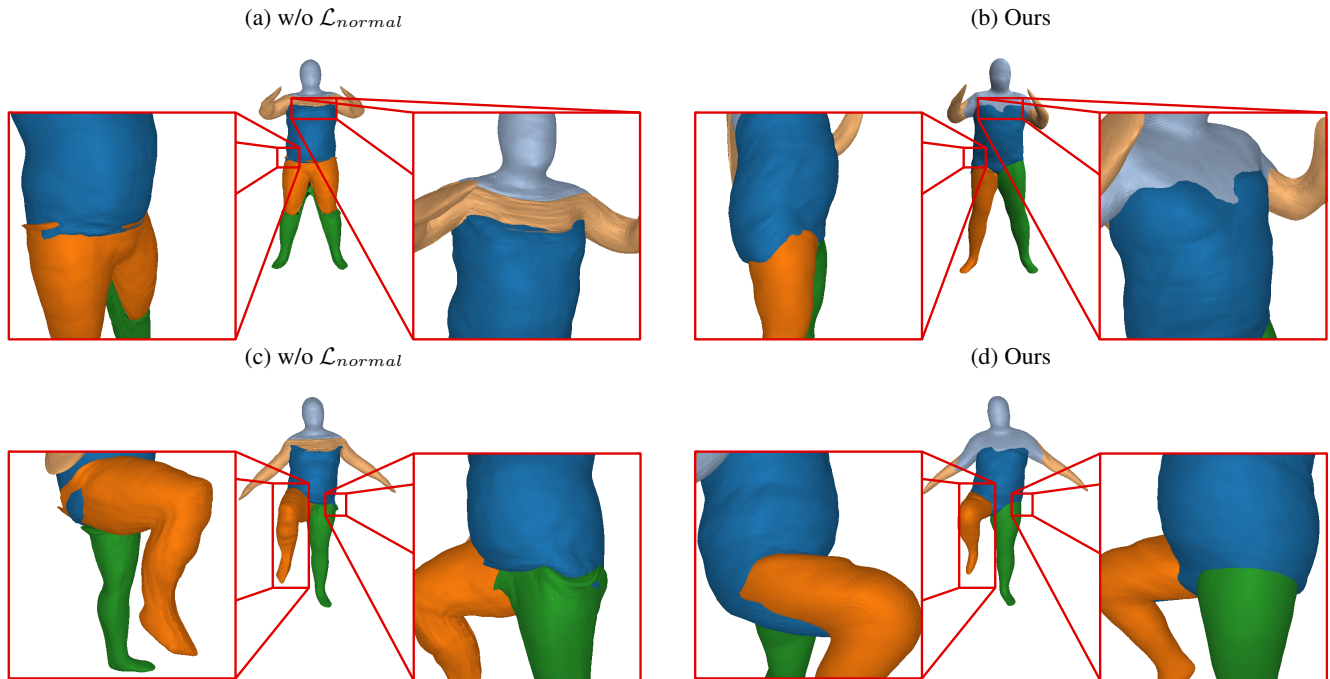


Figure 18: **Impact of  $\mathcal{L}_{norm}$ .** When removing the  $\mathcal{L}_{norm}$  from the optimization objective, the predicted primitives are semantically meaningful but the transitions between one primitive to another are not smooth i.e. do not have consistent normals. This becomes more evident when looking at the locations where primitives meet (marked with a red rectangle). In contrast, our model has smooth transitions and looks more “organic”.

**w/o Overlapping Loss:** The overlapping loss encourages semantically meaningful shape abstractions, where primitives represent distinct geometric parts. To this end, we introduce the  $\mathcal{L}_{overlap}(\mathcal{X}_o)$  loss (Eq. 15 in the main submission) to discourage having multiple primitives “containing” the same points from the target object. The reconstructions without the overlapping loss accurately capture the geometry of the human body but fail to yield semantically meaningful shape abstractions, since primitives completely penetrate one another (see Fig. 17). In Fig. 20, we visualize the predicted primitives for various humans and we notice that while they accurately capture the geometry of the human body, they do not correspond to meaningful geometric parts. In particular, there are 2 primitives that describe the right leg (primitive illustrated in blue and orange), 2 for the left leg (primitives illustrated in orange and green) and 3 for the main body (blue, light blue and green). Since, we want our primitives to correspond to semantic parts, this behaviour is not desirable.

**w/o Coverage Loss:** The coverage loss makes sure that all primitives will “cover” parts of the target object. In practice, it prevents primitives with minimal volume (see Fig. 22, fourth column) that do not contribute to the reconstruction. In Fig. 22, we note that when we remove  $\mathcal{L}_{cover}(\mathcal{X}_o)$  from our optimization objective, a primitive degenerates to a “sheet” that contains no points but only has surface area (Fig. 21).

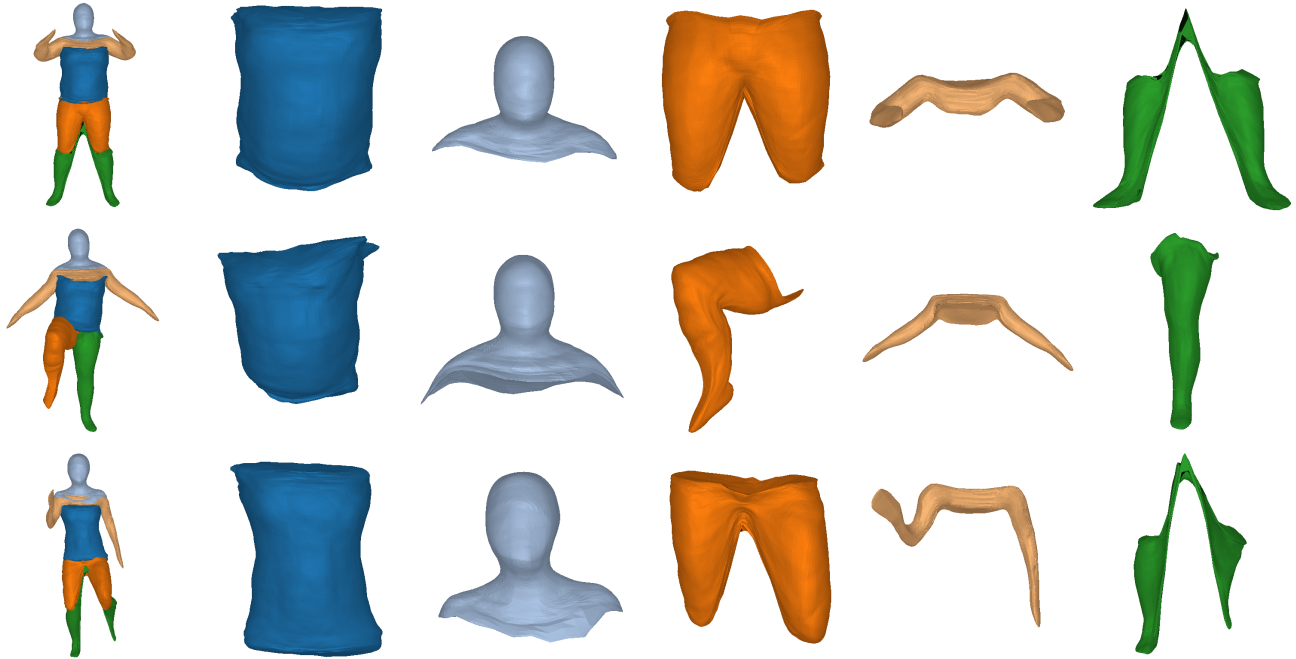


Figure 19: **w/o Normal Consistency Loss.** We visualize the predicted primitives when training without the  $\mathcal{L}_{normal}$  and we observe that even though the predicted primitives are expressive and have a semantic interpretation, the locations where the primitives meet do not have consistent normals.

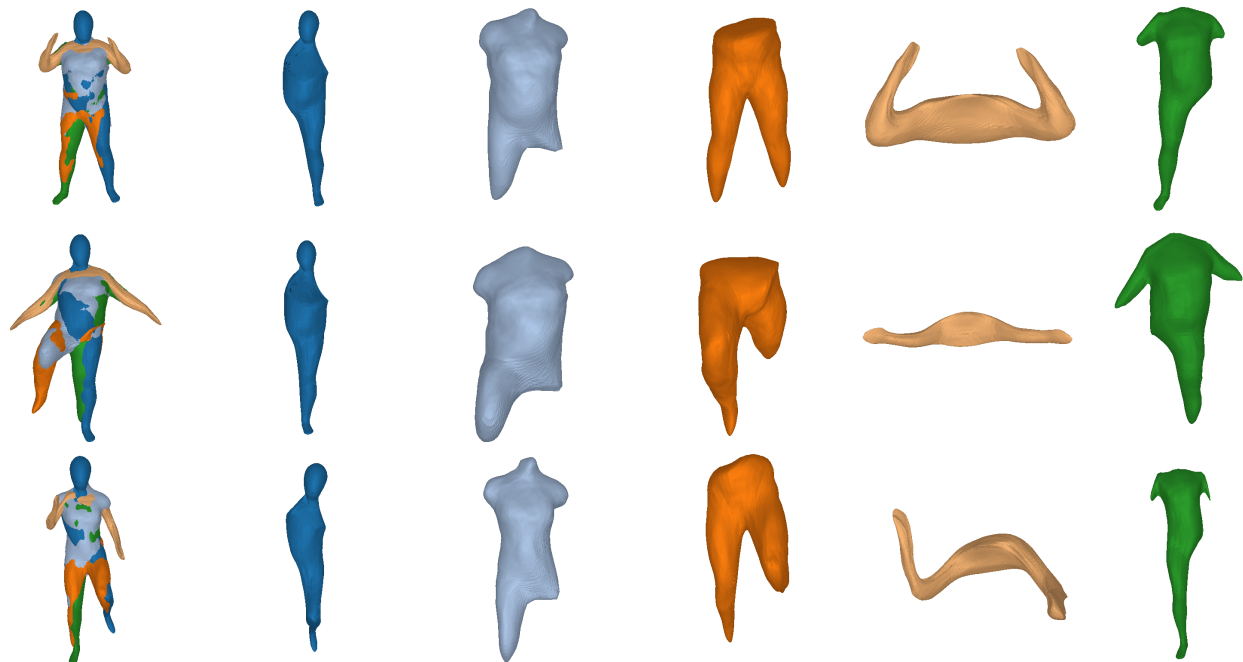


Figure 20: **w/o Overlapping Loss.** We visualize the predicted primitives when training without the  $\mathcal{L}_{overlap}$  and we observe that even though the predicted primitives are expressive and accurately capture the 3D geometry of the human body, they do not have a semantic interpretation, namely multiple primitives describe the same object part.

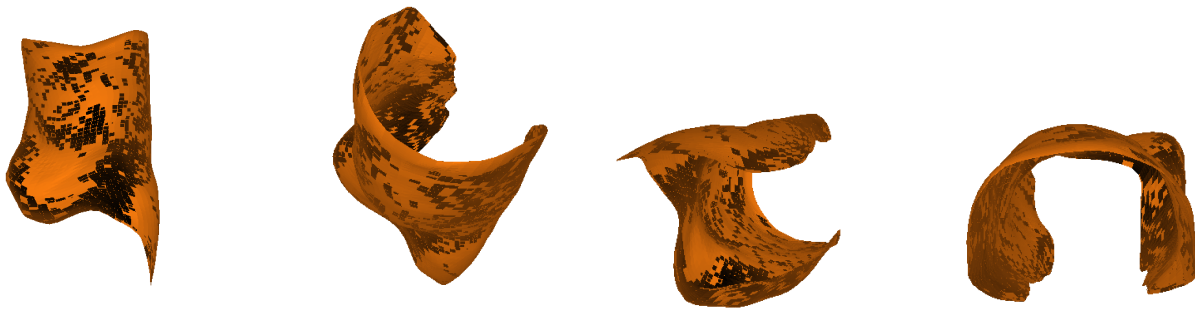


Figure 21: **Impact of  $\mathcal{L}_{cover}$ .** When removing the  $\mathcal{L}_{cover}$  some primitives become very thin (with minimum volume) and do not contribute to the reconstruction loss.

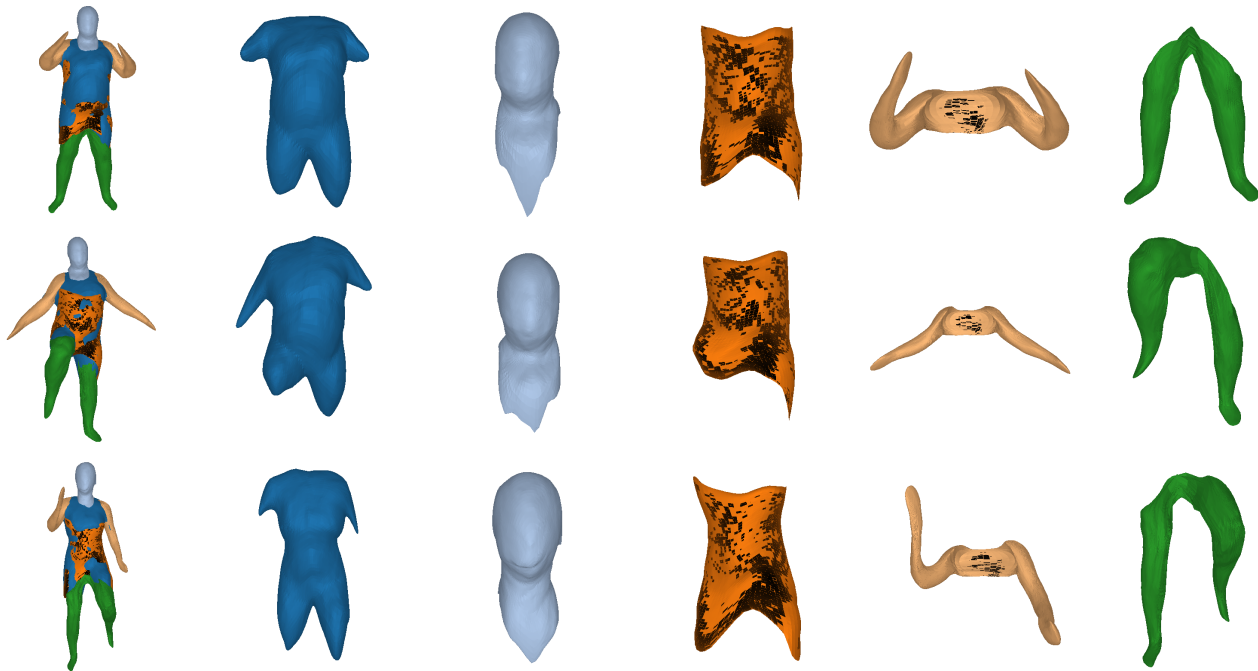


Figure 22: **w/o Coverage Loss.** We visualize the predicted primitives when training without the  $\mathcal{L}_{cover}$  and observe that although some of them are expressive and efficiently capture the 3D geometry, some primitives have minimum volume hence, do not cover parts of the object and in turn, do not contribute to the reconstruction loss.

## C. Experiment on D-FAUST

In this section, we provide additional information regarding our experiments on D-FAUST dataset [8]. D-FAUST contains 38,640 meshes of humans performing various tasks such as “chicken wings”, “running on spot”, “shake arms” etc. We follow [69] and use 70%, 20% and 10% for the train, test and validation splits. Furthermore, we filter out the first 20 frames for each sequence that contain the unnatural “neutral pose” necessary for calibration purposes. Note that in contrast to [69], we do not normalize the meshes to the unit cube in order to retain the variety of the human body i.e. tall and short humans. This makes the single view 3D reconstruction task harder, as all models need to efficiently capture both the pose and the size of the human.

Tab. 4 summarizes the quantitative results from Fig. 4 in our main submission. We notice that for all primitive-based baselines, increasing the number of parts results in improved reconstruction quality in terms of volumetric  $IoU$  and Chamfer- $L_1$  distance. Instead, Neural Parts, decouple the number of primitives from the reconstruction accuracy as the performance of our model is independent of the number of the predicted primitives. This is expected, since our primitives are highly expressive and our model can capture the 3D shape geometry using even a single primitive (see Fig. 23). We argue that this is a desirable property, as Neural Parts enable us to select the number of parts based on the expected number of semantic parts and not the desired reconstruction quality.

	OccNet	SQs				H-SQs				CvxNet				Ours				
		5	10	25	50	4	8	16	32	5	10	25	50	2	5	8	10	
IoU		0.691	0.514	0.565	0.616	0.607	0.559	0.595	0.623	0.610	0.582	0.607	0.622	0.621	0.675	0.673	0.676	0.678
Chamfer- $L_1$		0.102	0.147	0.129	0.114	0.116	0.161	0.148	0.126	0.129	0.183	0.161	0.139	0.121	0.101	0.097	0.090	0.095

Table 4: **Single Image Reconstruction on D-FAUST.** We report the volumetric  $IoU$  ( $\uparrow$ ) and the Chamfer- $L_1$  ( $\downarrow$ ) wrt. the ground-truth mesh for our model compared to primitive-based methods SQs [67] H-SQs [69], CvxNet [18] for various number of primitives and the non primitive-based OccNet [57]. We observe that our model outperforms all primitive-based baselines with only 2 primitives.

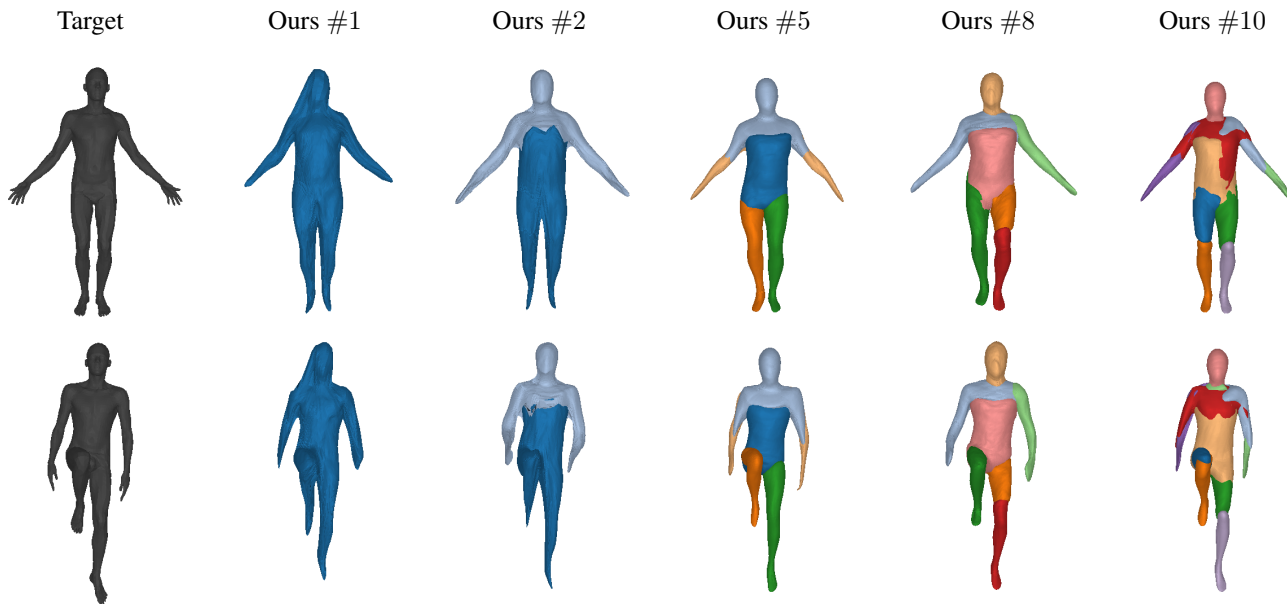


Figure 23: **Single Image 3D Reconstruction on D-FAUST.** The input image is shown on the first column and the rest contain predictions of our method with different number of primitives.

### C.1. Additional Experimental Results

In Fig. 24, we provide additional experimental results on the single-view 3D reconstruction task on D-FAUST. Similar, to the results in section 4.2 of the main submission, we compare our model with 5 primitives, with CvxNet and SQs with 50 primitives and H-SQs with 32 primitives. We observe that while CvxNet and H-SQs accurately capture the geometry of the human body, their predicted primitives lack any semantic interpretation, as primitives do not correspond to actual geometric



Figure 24: **Single Image 3D Reconstruction on D-FAUST**. The input image is shown on the first column and the rest contain predictions of all methods: OccNet (second), primitive-based predictions with superquadrics (third and fourth) and convexes (fifth) and ours with 5 primitives (last).

parts of the human body. Instead, SQs lead to semantic and parsimonious shape abstractions that are not accurate. On the other hand, Neural Parts achieve both semantic interpretability and high reconstruction quality.

## D. Experiment on FreiHAND

In this section, we provide additional information regarding our experiments on FreiHAND dataset [98]. For FreiHAND, we select the first 5000 hand poses and generate meshes using the provided MANO parameters [79]. We render them from a fixed orientation and use 70%, 20%, 10% for the train, test and validation splits. Note that MANO does not generate watertight meshes, thus we need to post-process the meshes in order to create occupancy pairs. This is achieved by adding triangular faces using the following vertex indices 38, 92, 234, 239, 279, 215, 214, 121, 78, 79, 108, 120, 119, 117, 118, 122.

### D.1. Additional Experimental Results

In Fig. 25, we provide additional qualitative results on the single-view 3D reconstruction task on FreiHAND. Similar to the results in section 4.2 of the main submission, we compare our model with 5 primitives to SQs and CvxNet with 5 primitives and H-SQs with 8. Note that for H-SQs we can only use a maximum number of primitives that is a power of 2. H-SQs with 4 primitives performed poorly; thus we increased the number of parts. We observe that Neural Parts yield semantically meaningful parts that accurately capture the hand geometry. Note that accurately modeling objects with non-rigid parts, such as the flexible human fingers, requires primitives that can bend arbitrarily (see thumb in second row Fig. 25). This is only possible with Neural Parts, as we do not impose any kind of constraint on the primitive shape.

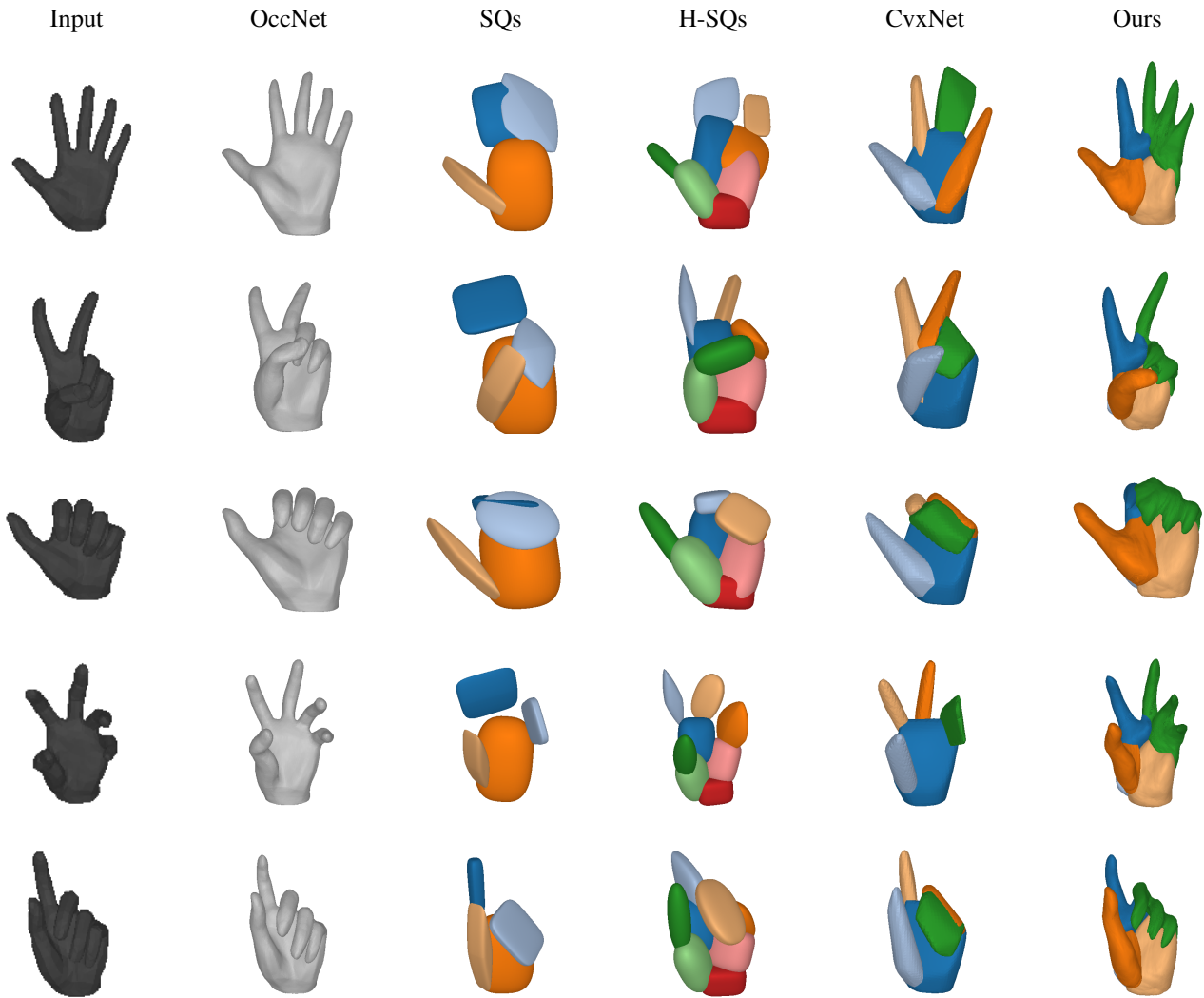


Figure 25: **Single Image 3D Reconstruction on FreiHAND.** We compare our model with OccNet, SQs and CvxNet with 5 primitives and H-SQs with 8 primitives.

## E. Experiment on ShapeNet

In this section, we provide additional information regarding our experiments on ShapeNet dataset [10]. In particular, we use the same image renderings and train/test splits of Choy et al. [16]. In order to determine whether points lie inside or outside the target mesh (i.e. for generating the occupancy pairs  $\mathcal{X}_o$ ) we need the meshes to be watertight. For this, we follow [57] and use the code provided by Stutz et al. [84]<sup>5</sup> which performs TSDF-fusion on random depth renderings of the object, to create watertight meshes of the object. In Fig. 26, we provide additional qualitative results on various ShapeNet cars and compare our model with 5 primitives to CvxNet with 5 and 25 and with the non primitive-based OccNet.

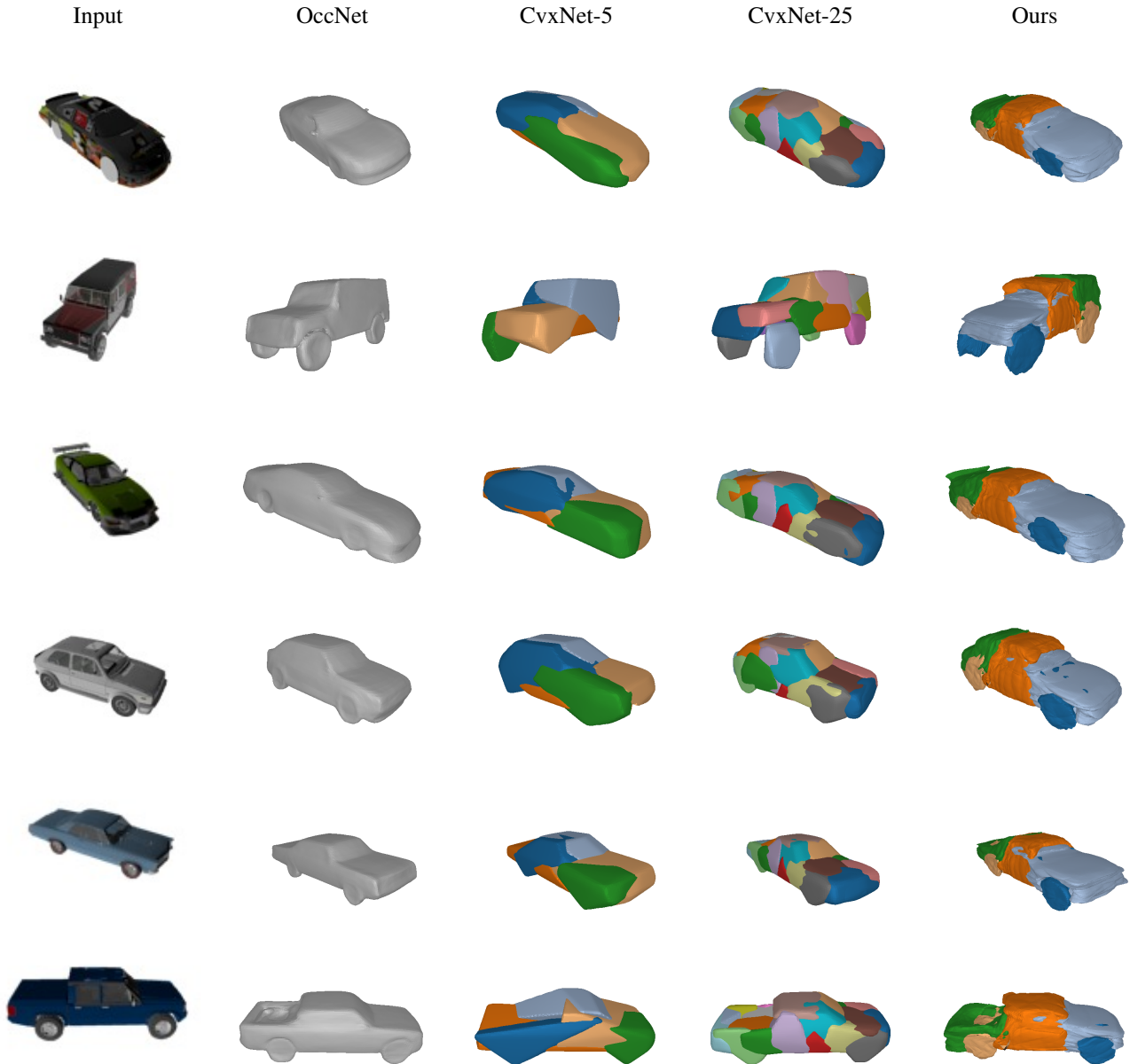


Figure 26: **Single Image 3D Reconstruction on ShapeNet.** We compare Neural Parts to OccNet and CvxNet with 5 and 25 primitives. Our model yields semantic and more accurate reconstructions with 5 times less primitives.

<sup>5</sup><https://github.com/davidstutz/mesh-fusion>

	OccNet	CvxNet - 5	CvxNet - 25	Ours
IoU	0.763	0.650	0.666	<b>0.697</b>
Chamfer- $L_1$	0.186	0.218	0.210	<b>0.185</b>

Table 5: **Single Image Reconstruction on ShapeNet cars.** Quantitative evaluation of our method against OccNet [57] and CvxNet [19] with 5 and 25 primitives.

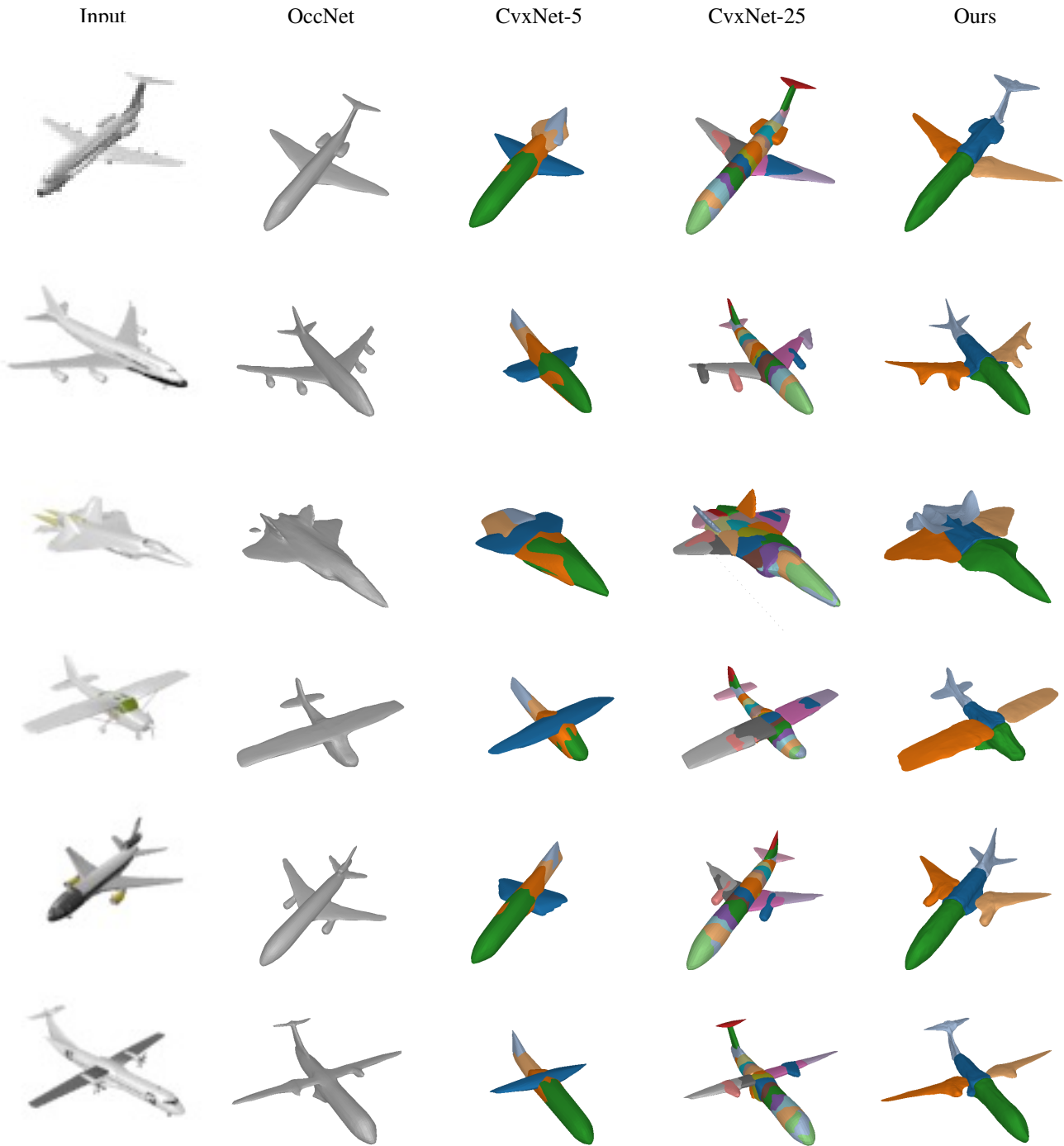


Figure 27: **Single Image 3D Reconstruction on ShapeNet.** We compare Neural Parts to OccNet and CvxNet with 5 and 25 primitives. Our model yields semantic and more accurate reconstructions with 5 times less primitives.

	OccNet	CvxNet - 5	CvxNet - 25	Ours
IoU	0.451	0.425	0.448	<b>0.454</b>
Chamfer- $L_1$	0.218	0.267	0.245	<b>0.220</b>

Table 6: **Single Image Reconstruction on ShapeNet airplanes.** Quantitative evaluation of our method against OccNet [57] and CvxNet [19] with 5 and 25 primitives.

Subsequently, we train Neural Parts with 5 primitives and compare with CvxNet with 5 and 25 primitives on ShapeNet planes (Fig. 27 + Tab. 6), ShapeNet lamps (Fig. 28 + Tab. 7) and ShapeNet chairs (Fig. 29 + Tab. 8). In Fig. 27, we provide a qualitative evaluation of our model with CvxNet and OccNet on various planes. We observe that Neural Parts yield more geometrically accurate and semantically meaningful shape abstractions than CvxNet with multiple primitives, i.e. the same primitive is consistently used for representing the tail and the wings of the airplanes. This is also validated quantitatively in Tab. 6, where we see that our model outperforms CvxNet in terms of IoU and Chamfer- $L_1$  both with 5 and 25 primitives. We observe that CvxNet with 5 primitives cannot represent fine details and as a result parts of the target object are not captured, e.g. the turbines of airplanes.

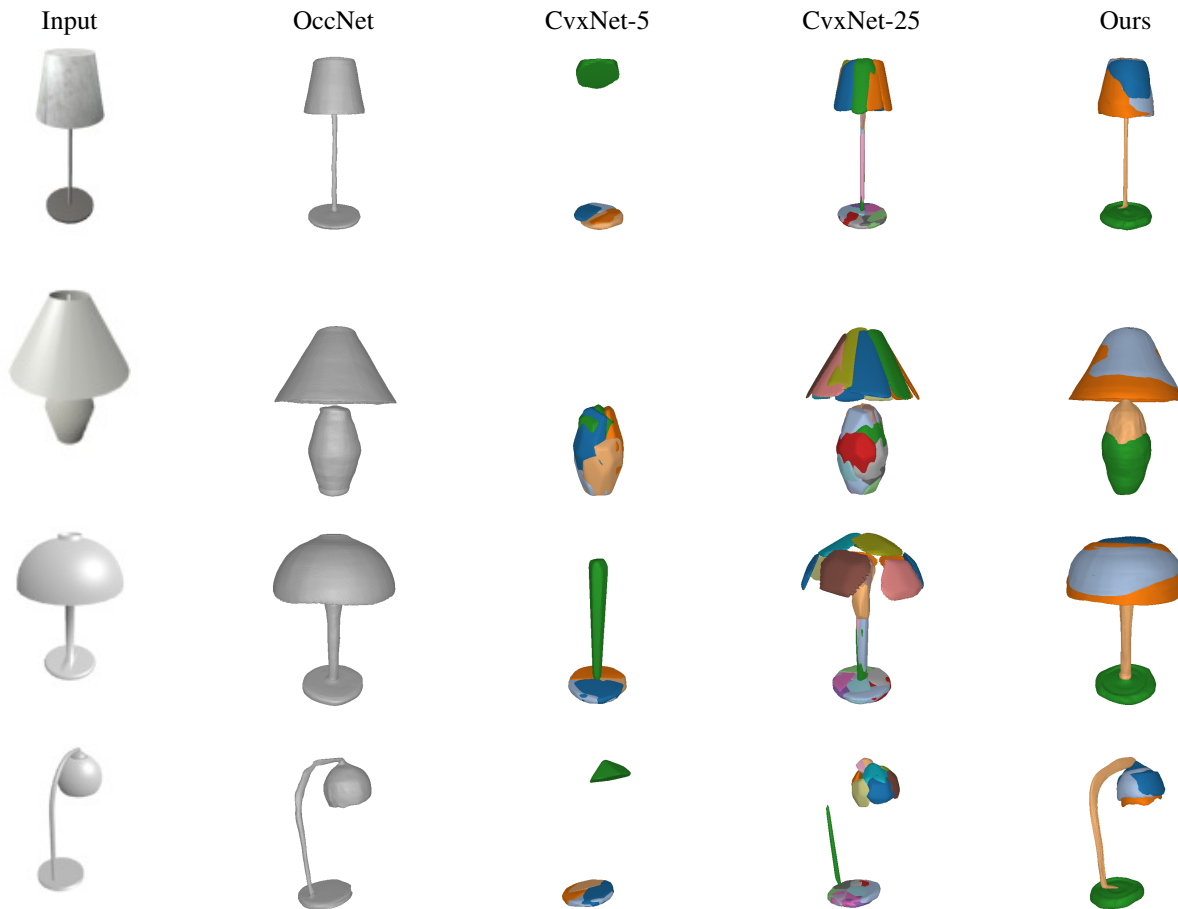


Figure 28: **Single Image 3D Reconstruction on ShapeNet.** We compare Neural Parts to OccNet and CvxNet with 5 and 25 primitives. Our model yields semantic and more accurate reconstructions with 5 times less primitives.

This becomes more evident for the case of lamps, where 5 primitives do not have enough representation power for modelling complex shapes such as the lamp shade or the lamp body (see Fig. 28 third column), thus entire object parts are missing. Similarly, also for the case of chairs, CvxNet with 5 primitives fail to accurately capture the object’s geometry (see Fig. 29 third column). For example, 5 primitives are not enough for representing the legs of the chair. Instead our model

	OccNet	CvxNet - 5	CvxNet - 25	Ours
IoU	0.339	0.246	0.278	<b>0.318</b>
Chamfer- $L_1$	0.514	0.613	0.537	<b>0.347</b>

Table 7: **Single Image Reconstruction on ShapeNet lamps.** Quantitative evaluation of our method against OccNet [57] and CvxNet [19] with 5 and 25 primitives.

with the same number of parts consistently captures the 3D geometry. On the contrary, CvxNet with 25 primitives yield more geometrically accurate reconstructions, however, the reconstructed primitives are not as semantically meaningful.

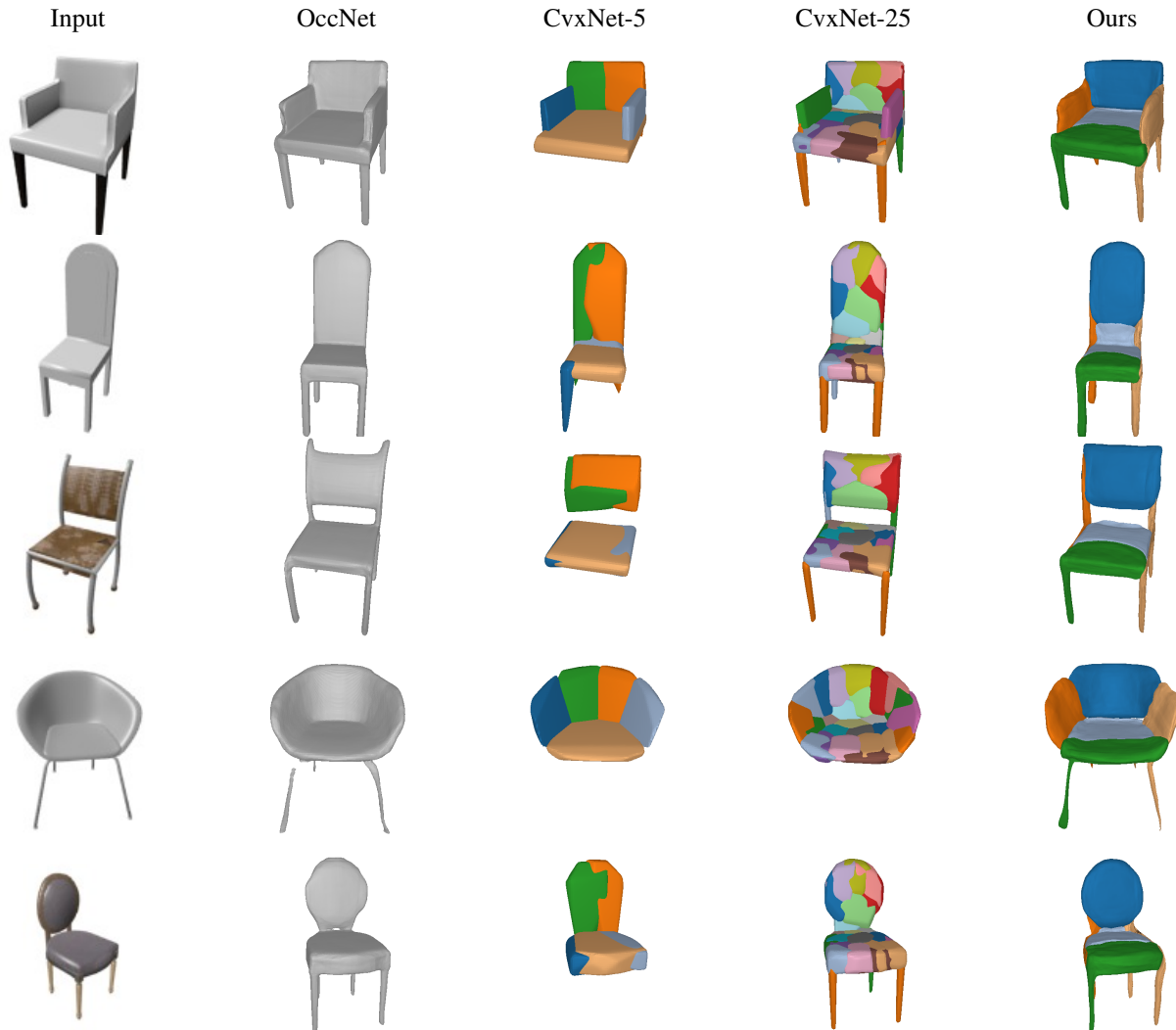


Figure 29: **Single Image 3D Reconstruction on ShapeNet.** We compare Neural Parts to OccNet and CvxNet with 5 and 25 primitives. Our model yields semantic and more accurate reconstructions with 5 times less primitives.

## F. Semantically Consistent Abstractions

In this section, we provide additional information regarding our Semantic Consistency experiment from Section 4.3 in our main submission. Furthermore, since D-FAUST contains 4D scans of humans in motion, we also evaluate the temporal consistency of the predicted primitives on various actions.

	OccNet	CvxNet - 5	CvxNet - 25	Ours
IoU	0.432	0.364	0.392	<b>0.412</b>
Chamfer- $L_1$	0.312	0.587	0.557	<b>0.337</b>

Table 8: **Single Image Reconstruction on ShapeNet chairs.** Quantitative evaluation of our method against OccNet [57] and CvxNet [19] with 5 and 25 primitives.



Figure 30: **Representation Consistency.** Our predicted primitives are consistently used for representing the same human part for different humans.

### F.1. Temporal Consistency

In this section, we provide a qualitative analysis on the temporal consistency of the predicted primitives. Results are summarized in Fig. 31. We observe that Neural Parts consistently use the same primitive for representing the same object

part regardless of the breadth of the part’s motion. Notably, this temporal consistency is an emergent property of our method and not one that is enforced with any kind of loss. Additional visualizations are provided in the supplementary video.

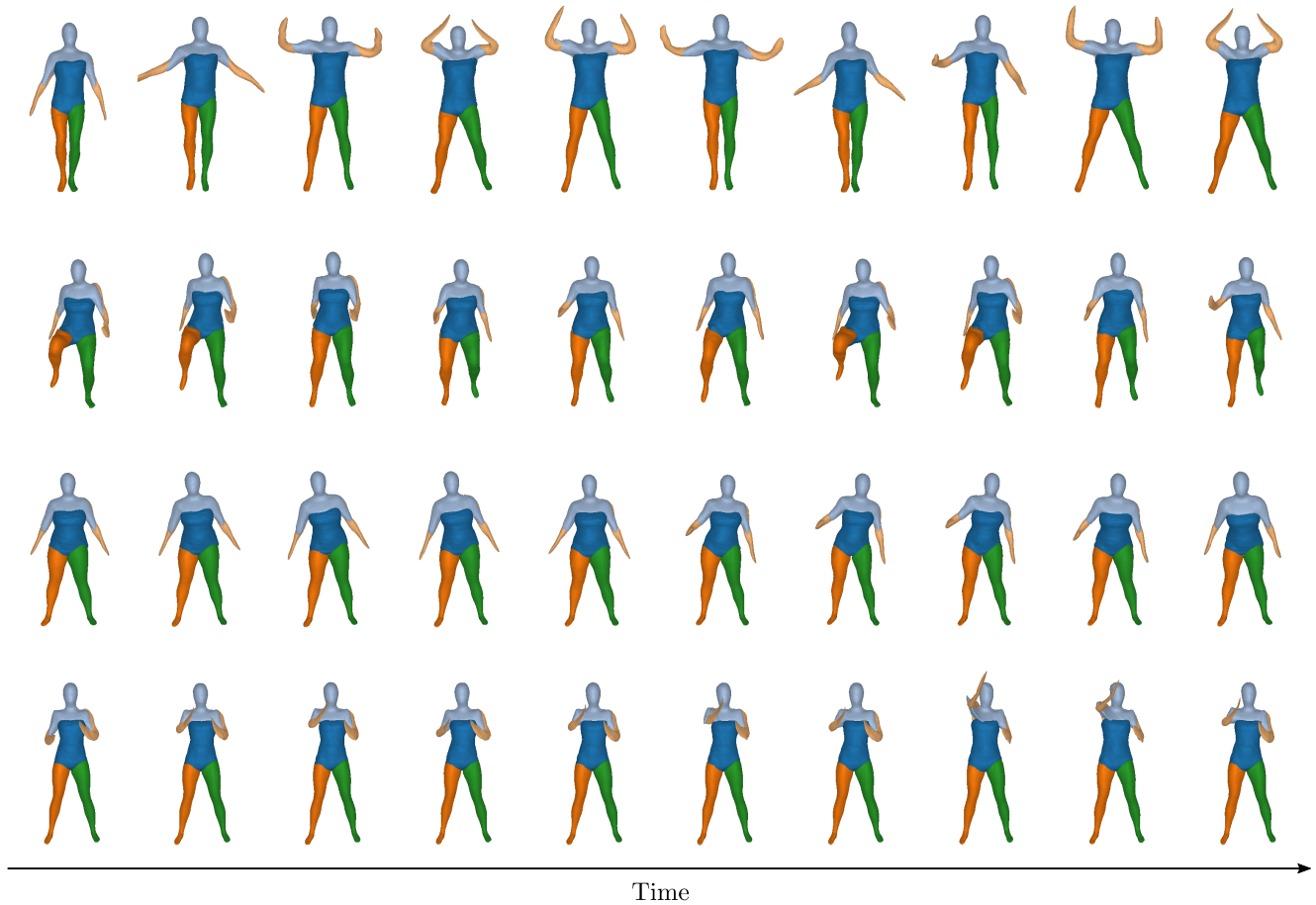


Figure 31: **Temporal Consistency of Predicted Primitives.** We note that Neural Parts yield primitives that preserve their semantic identity while different humans perform various actions.

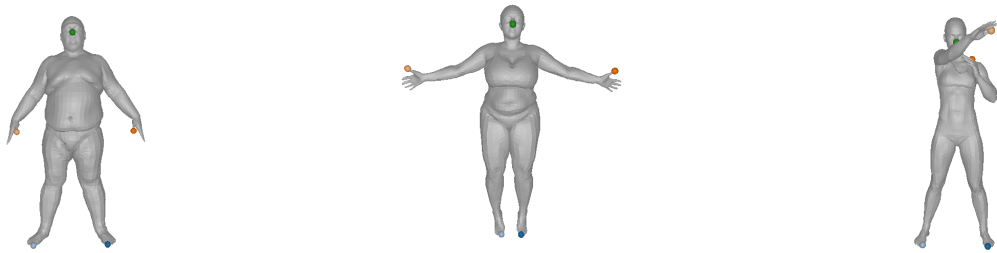


Figure 32: **Semantic vertices provided by SMPL-X.** We highlight the 5 vertex indices that we use to identify left thumb (L-thumb), right thumb (R-thumb), left toe (L-toe), right toe (R-toe) and nose.

## F.2. Semantic Consistency

In this experiment, we provide additional information regarding the Semantic Consistency experiment in our main submission (see Fig. 10). In particular, we evaluate whether a specific human part is represented consistently by the same primitive (see Fig. 30). To measure this quantitatively, we select 5 representative vertices on each target mesh (the vertex

indices are provided by SMPL-X [71]) and measure the classification accuracy of those points when using the label of the closest primitive. A visualization of the 5 vertices on the human body is given in Fig. 32. Note that the vertex indices are consistent across all subjects because D-FAUST meshes are generated using SMPL [54].